Impact of the Asian Monsoon Anticyclone on the Variability of mid-to-upper tropospheric methane above the Mediterranean Basin

P. Ricaud[1], B. Sič[1], L. El Amraoui[1], J.-L. Attié[1,2], R. Zbinden[1], P. Huszar[3], S. Szopa[4], J. Parmentier[1], N. Jaidan[1], M. Michou[1], R. Abida[1], F. Carminati[1,2,5], D. Hauglustaine[4,6], T. August[7], J. Warner[5], R. Imasu[8], N. Saitoh[9] and V.-H. Peuch[10]

[1]CNRM-GAME, Météo-France/CNRS UMR 3589, Toulouse, France

[2]Université de Toulouse, Laboratoire d'Aérologie, CNRS UMR 5560, Toulouse, France

[3]Department of Meteorology and Environment Protection, Faculty of Mathematics and Physics, Charles University, Prague, V Holešovičkách 2, Prague 8, 18000, Czech Republic

[4]Laboratoire des Sciences du Climat et de l'Environnement, CNRS UMR 1572, Gif sur Yvette, France

[5]University of Maryland, College Park, Maryland, USA

[6]Laboratoire Image Ville Environnement, CNRS UMR 7362, Strasbourg, France

[7]EUMETSAT, Darmstadt, Germany

[8]University of Tokyo, Tokyo, Japan

[9]Center for Environmental Remote Sensing, Chiba University, Japan

[10]European Centre for Medium-Range Weather Forecasts, Reading, UK

Correspondence to: P. Ricaud (philippe.ricaud@meteo.fr)

In revision, *Atmospheric Chemistry and Physics Discussions*

Version 14, 29 July 2014

Abstract

The space and time variabilities of methane (CH_4) total column and upper tropospheric mixing ratios are analyzed above the Mediterranean Basin (MB) as part of the Chemical and Aerosol Mediterranean Experiment (ChArMEx) programme. Since the analysis of the mid-to-upper tropospheric CH_4 distribution from spaceborne sensors and model outputs is challenging, we have adopted a climatological approach and have used a wide variety of datasets. We have combined spaceborne measurements from the Thermal And Near infrared Sensor for carbon Observations-Fourier Transform Spectrometer (TANSO-FTS) instrument on the Greenhouse gases Observing SATellite (GOSAT) satellite, the Atmospheric InfraRed Spectrometer (AIRS) on the AURA platform and the Infrared Atmospheric Sounder Interferometer (IASI) instrument aboard the MetOp-A platform with model results from the Chemical Transport Model (CTM) MOCAGE, and the Chemical Climate Models (CCMs) CNRM-AOCCM and LMDz-OR-INCA (according to different emission scenarios). In order to minimize systematic errors in the spaceborne measurements, we have only considered maritime pixels over the MB. The period of interest spans from 2008 to 2011 considering satellite and MOCAGE data and, regarding the CCMs, from 2001 to 2010. Although CH_4 is a long-lived tracer with lifetime of ~12 years supposed to be well mixed in the troposphere, an East-West gradient in CH_4 is observed and modelled in the mid-to-upper troposphere with a maximum in the Western MB in all seasons except in summer when CH_4 accumulates above the Eastern MB. The peak-to-peak amplitude of the East–West seasonal variation in CH_4 above the MB in the upper troposphere (300 hPa) is weak but almost twice greater in the satellite measurements (~25 ppbv) than in the model data (~15 ppbv). The maximum of CH_4 in summer above the Eastern MB can be explained by a series of dynamical processes only occurring in summer. The Asian monsoon traps and uplifts high amounts of CH_4 to the upper troposphere where they build up. The Asian Monsoon Anticyclone redistributes these elevated CH_4 amounts towards North Africa and Middle East to finally reach and descent in the Eastern MB. In

the lower troposphere, the CH_4 variability is mainly driven by the local sources of emission in the vicinity of the MB.

1. Introduction

During the last decades, major concerns have been caused by the impact and the role that atmospheric trace gases play in climate and air pollution changes and the crucial issue was to evaluate. In IPCC (2007), the ongoing changes of our atmosphere (composition, climate, air pollution, radiation) are reported. Among trace gases, methane (CH_4), carbon dioxide (CO_2), and nitrous oxide (N_2O) are predominant constituents which play an important role in atmospheric changes because they are strongly influenced by human activities. In the frame of predicting the future of the Earth's climate (IPCC, 2007), knowledge of today's CO_2, CH_4 and N_2O sources and sinks, spatial distribution and time variability is essential and this study will be dedicated to CH_4.

The net positive radiative impact of the human activity on climate, starting from 1750, has been evaluated to 1.6 [+0.6 to +2.4] Wm^{-2} (IPCC, 2007). In the atmosphere, the long-lived greenhouse gases account for 2.63 ± 0.26 Wm^{-2} and are the predominant radiative terms. CO_2, with tropospheric lifetime of 30–95 years, has a radiative efficiency of 1.4×10^{-5} $Wm^{-2}ppb^{-1}$, but CH_4 and N_2O, with tropospheric lifetimes of 12 and 114 years, respectively, are intensely more efficient by 3.7×10^{-4} and 3.03×10^{-3} $Wm^{-2}ppb^{-1}$, respectively. IPCC (2007) estimated CH_4 and N_2O to be responsible of 0.48 [+0.43 to 0.53] and 0.16 [+0.14 to 0.18] Wm^{-2}, respectively in the radiative forcing changes.

The Mediterranean Basin (MB) is located in a transitional zone between subtropical and mid-latitudes regimes (Lionello, 2012), highly sensitive to climate change. To illustrate, simulations tend to show a pronounced decrease in precipitation (2000-2100), especially in the warm season (Giorgi and Lionello, 2008), and Lionello (2012) reported on an observed summer West-East dissymmetry in precipitation (1979-2002). In terms of anthropogenic pollution sources, the MB is at the confluence of three continents, Europe, Africa and Asia. The impact of these distinct continental sources such as from manufactures and densely populated coastal areas (e.g. Marseille, Barcelona, Athens, Tunis, Cairo, Genoa or Roma) or forest fires (e.g. South East of France, Corsica, Portugal, Greece) is still not well understood, especially on the O_3 and CO budgets. Besides these

regional sources, polluted air masses may originate from Asia during the summer monsoon period, Africa through the Hadley cell and upper level anticyclone and North America through the westerlies. The “Expérience sur Site pour COntraindre les Modèles de Pollution atmosphérique et de Transport d'Emissions” (ESCOMPTE) campaign (June-July 2001) in southeastern France aimed to characterize the summer time pollution events over there (Cros et al., 2004). The goal of the Mediterranean Intensive Oxidant Study (MINOS) campaign (July-August 2001) in the eastern Mediterranean was to measure long-range transport of air pollution and aerosols from South East Asia and Europe towards the MB (Ladstätter-Weißenmayer et al.,, 2003; Scheeren et al., 2003). They have demonstrated the importance of coastal and synoptic transport mechanisms on the variability of constituents but were not adapted to assess the budgets of O_3, CO and long-lived species.

The ChArMEx (Chemistry and Aerosol Mediterranean Experiment) Project (http://charmex.lsce.ipsl.fr/) is the atmospheric chemistry component of a large multidisciplinary Mediterranean regional program proposed and conducted by France. It intends, among other objectives, to quantify processes explaining the temporal evolution of chemical compounds and aerosols in the troposphere above the Mediterranean Basin (MB). To achieve these goals over the first phase (2010-2015), the program uses data from satellites, ground-based, sondes, aircraft, models and assimilation in order to evaluate 1) the variabilities and recent trends of several species (e.g. O_3, CO, N_2O) and aerosols, 2) the synoptic-scale circulation that controls their transport, and 3) the future chemical climate over the MB by 2100.

We have to keep in mind that it is rather challenging 1) to measure long-lived species from space focusing on tropospheric layers and 2) to model these molecules over the entire troposphere. Concentrations of long-lived atmospheric chemical species (CO_2, CH_4, and N_2O) are expected to be very well-mixed and evenly distributed throughout the lower atmosphere. The past/present nadir-viewing instruments able to actually measure CH_4 in the troposphere have been/are:

1) the Interferometric Monitor for Greenhouse gases (IMG) instrument operating in the Thermal Infrared (TIR) aboard the ADvanced Earth Observing Satellite (ADEOS-1) platform in 1996-1997 (Clerbaux et al., 1998);

2) the near-IR (NIR) Scanning Imaging Absorption Spectrometer for Atmospheric Chartography (SCIAMACHY) aboard the ENVIronment SATellite (ENVISAT) platform (Buchwitz et al., 2000) from 2002 to 2012;

3) the Tropospheric Emission Spectrometer (TES) operating in the TIR aboard the Aura platform (Worden et al., 2012) from 2004 to date;

4) the Thermal And Near infrared Sensor for carbon Observations – Fourier Transform Spectrometer (TANSO-FTS) on the Greenhouse gases Observing SATellite (GOSAT) platform (Yokota et al., 2009) both in the Short-Wave InfraRed (SWIR) and in the TIR from 2008 to date;

5) the Atmospheric InfraRed Sounder (AIRS) aboard the Aqua platform (Xiong et al., 2008) measuring in the TIR from 2004 to date;

6) the Infrared Atmospheric Sounding Interferometer (IASI) instrument aboard the MetOp-A and -B platforms (Hilton et al., 2012) operating in the TIR from 2008 to date, and aboard the MetOp-C platform expected to be launched in 2016.

Table 1 synthesizes the above mentioned information and shows the nadir-viewing instrument capability to measure tropospheric CH_4. The sensitivity of the TIR to measure CH_4 is rather weak except on areas showing a high thermal contrast at the surface (vertical gradient of temperature between the surface and the lowermost planetary boundary layer) as the ones encountered over the tropics (Crevoisier et al., 2013) contrarily to the measurements performed in the SWIR (Yoshida et al., 2013). In the NIR, analyses are essentially restricted to areas over land because the retrievals over sea are considered less reliable due to fairly low surface albedo of water, which results in low signals and thus in low signal-to-noise ratios (Georgoulias et al., 2011).

In parallel to the satellite data, models have also been used in order to assess the variability, sources and sinks, and future trends of the long-lived species. Examples are: CH_4 emission and flux

estimates at global scales (Bergamaschi et al., 2009; Bousquet et al., 2011), future evolution of long-lived species included in the international Atmospheric Chemistry and Climate Model Intercomparison Project (ACCMIP) involving more than 10 different models (Lamarque et al., 2013).

Numerous studies have examined the variabilities of atmospheric compounds above the MB to highlight the processes (sources and sinks) associated by coupling surface, balloon-borne, airborne, spaceborne measurements with models results at different scales, from mesoscales to global scales. Constituents are for instance aerosols (Nabat et al., 2012), radionuclides (Masson et al., 2010), ozone (Liu et al., 2009), carbon monoxide (Drori et al., 2012). The impact of 1) the different meteorological regimes and 2) the seasonal variabilities of the emissions of atmospheric constituents, e.g. CO emitted from fires in summers, produces a seasonal variation in all the constituents. It also produces a longitudinal gradient between the Eastern and the Western MB, together with a seasonal variation in the gradient. For example, European anthropogenic emissions were found to significantly influence the Eastern MB surface CO concentrations, while European biomass burning emissions were found to have only a small impact on Eastern MB surface CO concentrations (Drori et al., 2012). Total columns of CH_4 as measured by SCIAMACHY over land and the Eastern Mediterranean from 2003 to 2004 show latitudinal and seasonal variations that cannot be attributed to volcano eruptions (Georgoulias et al., 2011).

The aim of the present paper is to assess the variability of CH_4 in the mid-to-upper troposphere between the East and the West of the Mediterranean Basin and to attribute the seasonal variability of the East-West gradient to different processes at both, synoptic and global scales depending on the season and the altitude layer considered. We will study in detail the impact of the summer-time long-range transport of CH_4 from Asia to the Eastern MB through the Asian Monsoon Anticyclone. Since we have already underlined that measurement and modeling of the tropospheric CH_4 distribution are challenging, we will adopt a climatological approach and will use a wide variety of space-borne measurements and model outputs to verify that they give consistent results. Our

approach is thus based on three different models: the CTM MOCAGE (Josse et al., 2004) and the two Chemical Climate Models (CCMs) CNRM-AOCCM from Météo-France (Huszar et al., 2013) and LMDz-OR-INCA (Hauglustaine et al., 2004; Szopa et al., 2013) from the Laboratoire des Sciences du Climat et de l'Environnement (LSCE). To complete, we have considered the CH_4 profiles from AIRS and GOSAT, and the CH_4 total columns from IASI.

The manuscript is structured as follow. In section 2, we briefly present the spaceborne instruments and datasets involved in this study, namely MetOp-A/IASI, AQUA/AIRS and GOSAT/TANSO together with the models, namely MOCAGE, CNRM-AOCCM and LMDz-OR-INCA. The meteorology and climatology of CH_4 inferred from the different datasets above the MB are discussed in section 3. The CH_4 variability both in the East and in the West of the MB is presented in section 4. A detailed discussion of the different processes involved in the CH_4 variability above the MB is presented in section 5 underlining the impact of the Asian Monsoon Anticyclone to the distribution of the mid-to-upper CH_4 in the Eastern MB. Finally, section 6 concludes the paper.

2. The datasets

2.1. The satellite data

Our CH_4 study from satellite data analyses measurements from three different spaceborne TIR sensors (IASI, AIRS and GOSAT) by only considering the pixels over the Mediterranean Sea in order to minimize the systematic biases among pixels (day vs. night, land vs. sea). The sensitivity of TIR retrievals strongly depends on surface parameters: emissivity, temperature and thermal contrast (Claeyman et al., 2011). Compared to land surface, sea surface emissivity is relatively smaller in magnitude and more spatially uniform. Sea surface temperature exhibits a diurnal amplitude weaker than land surface temperature. Therefore, the vertical sensitivity of the TIR measurements, defined as the full-width at half-maximum of the averaging kernels from the optimal estimation method (Rodgers, 2000), over the sea is consistent during day and night and concentrated in the mid-

troposphere. Over the land, the vertical sensitivity is, on average, lower in the middle troposphere during the day than during the night, depending on the actual value of the thermal contrast at the surface.

Infrared sounders measurement errors can be rather large, e.g. up to 10% or more for a single CH_4 total column IASI pixel (Turquety et al., 2004). Thus, by the use of time (monthly/seasonally) and geographical averages, including more than a thousand measurements, we can lower the random error to less than 1%. Systematic errors, if any, will of course be unchanged. For that reason, our analysis relies on a differential method to highlight the CH_4 variability by considering the difference between the Eastern MB (EMB) and the Western MB (WMB), assuming that the systematic errors are of the same order of magnitude (although partially unknown) within each geographical box that will be defined in section 3.

2.1.1. The IASI data

IASI, on board of MetOp-A, was launched in 2006 by the European Organisation for the Exploitation of Meteorological Satellites (EUMETSAT). More specifications on platform and instrument can be found on http://smsc.cnes.fr/IASI and http://www.eumetsat.int/Home/Main/Satellites/Metop/Instruments/SP_2010053151047495). The retrieval algorithm for CH_4 is based on the neural network theory adapted from Turquety et al. (2004). The retrieval method is embedded in the operational IASI Level 2 product processing facility at EUMETSAT (EUMETSAT, 2004; Schlüssel et al., 2005, August et al., 2012). From the spectral bandwidth 1230-1347 cm^{-1}, the estimated accuracy of the CH_4 total column is about 2% and the estimated precision is of the order of 10% (Turquety et al., 2004). The true accuracy cannot be stated without reference to independent means of comparison, which are not available so far. Consequently, we consider a random Gaussian error of ~10% associated with each single pixel of retrieved total column of CH_4. At mid-latitudes, the vertical sensitivity of the total column CH_4 is peaking in the mid-troposphere at ~8 km from 4 to 14 km (Razavi et al., 2009) and, in the tropics, at ~10 km from

5 to 15 km. Geophysical level 2 pre-operational data are provided by EUMETSAT (from version 4 to version 5 from 2008 to 2011). The CH_4 products, not yet validated, are only experimental products, routinely generated for demonstration and evaluation. Note, the number of daily total columns of CH_4 averaged in a 1°x1° bin is highly variable because of cloud-free IASI considerations. The monthly-averaged IASI data within each of the East and West areas defined in section 3 represent an average of 30000-70000 pixels depending on the month considered.

2.1.2. The AIRS data

AIRS is onboard the space platform NASA EOS Aqua, launched in 2002 (http://airs.jpl.nasa.gov/). AIRS measures approximately 200 channels in the 7.66 μm absorption band of CH_4, of which 71 channels are used to retrieve CH_4. A detailed description of the retrieval algorithm can be found in Susskind et al. (2011). Note, the averaging kernels provided by NASA will be considered further (section 4.2) in order to degrade the vertical resolution of the model outputs. At mid-latitudes, the most sensitive layer of AIRS channels to CH_4 is at 300 hPa (~9 km) with a vertical sensitivity from 700 to 100 hPa (Xiong et al., 2008), and, in the tropics, at 200 hPa from 500 to 70 hPa consistently with the IASI TIR measurement sensitivity. Around 200-300 hPa, considering the version V5 used in the present analysis (Xiong et al., 2008), the precision of AIRS CH_4 is estimated to be 30 ppbv (1.7%) and validation using in situ aircraft measurements shows that the accuracy of the retrieved CH_4 is 0.5–1.6%. Daily maritime profiles of CH_4 have been averaged in 1°x1° bins over the MB. The monthly-averaged AIRS data within each of the East and West areas defined in section 3 represent an average of 6000-10000 vertical profiles depending on the month considered.

2.1.3. The GOSAT data

The Japanese Aerospace Exploration agency (JAXA) launched the GOSAT platform in 2009, with the TANSO-FTS spectrometer, a nadir-viewing instrument designed for greenhouse gases

research, CO_2 and CH_4, operating in the TIR and SWIR domains [0.7-14.3 μm] (Kuze et al., 2009). More specifications on platform and instrument can be found on http://www.gosat.nies.go.jp/. The sensitivity of the SWIR CH_4 measurements at 1.67 μm (Yokota et al., 2009) at mid-latitudes over the sea is very weak, thus few meaningful pixels could have been retrieved preventing the use of such information in our analysis. The TIR measurements from Band 4 (5.5–4.3 μm) provide vertical profiles of CH_4 along 7 vertical levels (Imasu et al., 2007) by using the optimal estimation method with a vertical sensitivity in the tropics peaking at 10 km (higher than at mid-latitudes) from 5 to 15 km (Saitoh et al., 2012), consistently with the vertical sensitivity of IASI (Razavi et al., 2009) and AIRS (Xiong et al., 2008) in the tropics. A selection by using Degree of Freedom of Signal (DFS) is applied for the data having DFS values larger than 0.6 for CH_4. TIR data (L2 Version 0.10) were only available from 16 March to 24 November 2010 from the GOSAT User Interface Gateway at the time the analysis has been performed. These retrievals provide vertical profiles of mixing ratio of CH_4 from 1000 to 100 hPa. Comparisons with aircraft measurements show that the average difference between the GOSAT (TIR) and aircraft CH_4 values (TIR − aircraft) is −5 ppbv, and the 1σ standard deviation is 15 ppbv (Saitoh et al., 2012). Daily maritime profiles of CH_4 have been averaged in 1°x1° bins over the MB. The monthly-averaged GOSAT data within each of the East and West areas defined in section 3 represent an average of 100-300 vertical profiles depending on the month considered, namely 20-30 times less than for AIRS.

2.2. The model data

2.2.1. The MOCAGE data

MOCAGE (MOdèle de Chimie Atmosphérique à Grande Echelle) (Peuch et al., 1999) is a 3D CTM which covers the planetary boundary layer, the free troposphere, and the stratosphere for different applications such as: operational chemical weather forecasting (Dufour et al., 2005); tropospheric and stratospheric research studies (Claeyman et al., 2010; Ricaud et al., 2009); and data assimilation research (El Amraoui et al., 2010; Claeyman et al., 2011). In our study, MOCAGE

is forced dynamically by wind and temperature fields from the analyses of the ARPEGE model (Courtier et al., 1991). The MOCAGE horizontal resolution is 2°x2° and the model uses a semi-Lagrangian transport scheme. It includes 47 levels from the surface up to 5 hPa with a vertical resolution of about 800 m around the tropopause, 400-800 m in the troposphere and 40-400 m in the 7 levels of the boundary layer. Chemistry used within MOCAGE is a combination of tropospheric (RACM described in Stockwell et al., 1997) and stratospheric (REPROBUS described in Lefèvre et al., 1994) chemical schemes. Initial chemical conditions are taken from climatological fields over a spin-up period of 3 months allowing the model to quickly bring chemical fields to realistic spatial distributions. Surface emissions prescribed in MOCAGE are based upon yearly- or monthly-averaged climatologies. More precisely, the CH_4 surface emissions are monthly averages and split into anthropogenic sources taken from the Intergovernmental Panel on Climate Change (IPCC) (Dentener et al., 2005), biomass burning (van de Werf et al., 2003) and biogenic sources (Michou and Peuch, 2002). The CH_4 climatologies are representative of year 2000 for a total emission rate of 534 $Tg(CH_4)\ yr^{-1}$.

2.2.2. The CNRM-AOCCM data

The atmospheric model embedded in CNRM-AOCCM is presented in Huszar et al. (2013) based on the Atmosphere-Ocean General Circulation Model (AOGCM) CNRM-CM5 described in Voldoire et al. (2012). The main difference between CNRM-CM5 and CNRM-AOCCM resides in the “online” coupling with a stratospheric chemistry which is based on the REPROBUS scheme. This scheme is applied on the whole vertical column, except between the surface and the 560 hPa level where long-lived chemical species are relaxed towards global average surface value following the A1B scenario from IPCC (2007). The A1B scenario mainly describes a future world of very rapid economic growth, global population that peaks in mid-century and declines thereafter, and the rapid introduction of new and more efficient technologies. Convection of species is not considered. In this chemistry version, the 3-D distribution of the seven absorbing gases (H_2O, CO_2, O_3, CH_4,

N_2O, CFC11, and CFC12) is then provided by the chemistry module of CNRM-AOCCM and interacts with the radiative calculations. More details can be found in Michou et al. (2011). In the present version, there are about 50 chemical species, and the horizontal resolution is 2.8°x2.8°. Distribution of atmospheric constituents at the surface are zonally symmetric below 500 hPa (Fig. 10) and greenhouse gases follow the A1B scenario on atmospheric chemistry and climate for the period of 1940-2100. In the present analysis, for this model, we only consider the climatological period 2001-2010.

2.2.3. The LMDz-OR-INCA data

The INteraction between Chemistry and Aerosol (INCA) model is used to simulate the distribution of aerosols and gaseous reactive species in the troposphere. In the present configuration, the model includes 19 hybrid vertical levels extending up to 4 hPa, and a horizontal resolution of 1.9° in latitude and 3.75° in longitude. INCA is coupled online to the LMDz General Circulation Model (GCM) to account, with different degrees of complexity, for climate chemistry interactions. In the simulations described here, LMDz is coupled with the ORCHIDEE (Organizing Carbon and Hydrology in Dynamic Ecosystems) dynamic global vegetation model (Krinner et al., 2005) for soil/atmosphere exchanges of water and energy (Hourdin et al., 2006), but not for biogenic CO_2 or Volatile Organic Compounds (VOCs) fluxes. Together, these three models form the LMDz-OR-INCA model. Fundamentals for the gas phase chemistry are presented in Hauglustaine et al. (2004) and first results with the full tropospheric gaseous chemical scheme are presented by Folberth et al. (2006). The model includes 223 homogeneous chemical reactions, 43 photolytic reactions and 6 heterogeneous reactions including non-methane hydrocarbon oxidation pathways and aerosol formation. The LMDz-OR-INCA simulation covers four future projections of emissions for the 2000–2100 period. The Representative Concentration Pathways (RCP) emissions are used (Lamarque et al., 2011). They correspond to emission trajectories compatible with the evolution of radiative forcing equivalent in 2100 to 2.6, 4.5, 6.0 and 8.5 Wm^{-2} relative to pre-

310 industrial values (labelled therein after RCP 2.6, 4.5, 6.0 and 8.5). In the present analysis, for this
311 model, we only consider the climatological period 2001-2010.
312

313 ## 3. Atmospheric conditions controlling the spatial distribution of methane

314 Figure 1 shows the CH_4 fields calculated by MOCAGE for summer (June-July-August, JJA)
315 2009 over the MB at 850, 500 and 200 hPa, superimposed with the wind fields from the ARPEGE
316 analyses averaged over the same period. Figure 2 presents the CH_4 vertical distribution as
317 calculated by MOCAGE in summer 2009 along an East-West axis above the MB. Similarly to
318 Figures 1-2, the Figures 3-4 present, in winter (December-January-February, DJF) 2009, the CH_4
319 fields as calculated by MOCAGE over the MB at 850, 500 and 200 hPa, and along an East-West
320 axis, respectively. On Figures 2 and 4, the MOCAGE CH_4 fields are superimposed with 1) the wind
321 fields from ARPEGE analyses and 2) the cold point tropopause pressure fields provided by the
322 National Oceanic and Atmospheric Administration (NOAA) National Centers for Environmental
323 Prediction (NCEP)/National Center for Atmospheric Research (NCAR) reanalyses, all these data
324 being averaged over the same period.
325 Considering the meteorology of the MB, we observe two different regimes. 1) In winter, and
326 more generally from autumn to spring (not shown), from the boundary layer to the upper
327 troposphere, air masses are essentially coming from either Europe or Eastern Atlantic Ocean. 2) In
328 summer, the meteorology of EMB and WMB is more complex and depends on the altitude
329 considered.
330 In the planetary boundary layer, cells develop in the WMB, and air masses come from Europe,
331 Northern Africa and Eastern Atlantic Ocean, whilst in the EMB, air masses are originated from four
332 major source regions: i) long fetch of maritime European air masses from NW throughout the whole
333 year, ii) North east continental flow originating in south Eastern Europe (Etesian winds) in summer,
334 iii) South-east flow from the Arabian Peninsula occurring in the fall, and iv) South-west flow along
335 the North-African coast most frequent during late winter and spring (Dayan, 1986). In the middle

troposphere, whatever the season, air masses are essentially coming from the west for both parts of the basin. In summer, upper tropospheric air masses in the WMB are essentially coming from the West, but in the EMB, they are also originated from Northern Africa and the Arabic Peninsula (Ziv et al., 2004; Liu et al., 2009), and even farther away, from Asia (we will discuss this point in sections 4 and 5). Note that, in summer, the EMB and WMB are also affected by the location of the descending branch of the Hadley cell. These summer climatologies are all consistent with Millán et al. (1997), Lelieveld et al. (2002), Ziv et al. (2004) and Schicker et al. (2010).

Seasonally-averaged wind fields from ARPEGE analyses show two different regimes in the surface pressure values during the summer and the winter periods. During the summer in the WMB, there is a higher pressure regime than in the EMB. In the lowermost troposphere (850 hPa), an anticyclonic cell develops in the WMB that has an impact on the distribution of CH_4 by producing a local minimum (Fig. 1). At 850 hPa, air masses are coming from Europe, North Africa and the Atlantic Ocean. The CH_4 distribution shows a maximum over Europe, consistently with the strongest emission zones (Fig. 10), and a strong minimum over North Africa. In the mid-troposphere (500 hPa), air masses are coming from Europe, and the Atlantic Ocean. An East-West gradient is detected with more CH_4 on the EMB. In the upper troposphere (200 hPa), air masses are originated from the Atlantic Ocean (even North America) and from North Africa and Asia producing over the MB an obvious North-South gradient with more CH_4 in the South (upper troposphere) than in the North (lower stratosphere) attributed to the impact of long-range transport of pollutants (as discussed in section 5). A systematic subsidence is present over the MB (Fig. 2) whatever the longitudinal bin considered due to the presence of semi-permanent subtropical high pressure systems which are centred over the tropical deserts. More precisely, in the WMB, the descent is caused by the presence of a high pressure cell (Fig. 1) whilst, in the EMB, it is coming from the Hadley cell that is further displaced over the Northern Africa producing a downward branch in the area 30°N-35°N. The tropopause moves up from ~200 hPa in the WMB to ~175 hPa in the EMB. The CH_4 distribution shows 1) an obvious transition at the tropopause and 2) a

362 minimum in the West and a maximum in the East in the low troposphere accentuated by the
363 systematic descent in the Eastern MB that brings CH_4-enriched air masses from the upper
364 troposphere to the mid-to-low troposphere.

365 In winter, the meteorological condition of the MB is much more homogeneous with westerlies
366 blowing whatever the pressure considered from 850 to 200 hPa (Figs. 3-4). North-South (and to a
367 lesser extent East-West) gradients in CH_4 can also be detected (Fig. 3) associated to the local
368 sources of emission over Europe at 850 hPa and to the stratosphere/troposphere transition at 200
369 hPa. The 500-hPa layer is a transition region between the low and the upper troposphere with
370 minima of CH_4 over North Africa and a cell of high CH_4 in the WMB. Contrarily to summer, since
371 the temperature of the Mediterranean Sea is greater than that of the surrounding continents, a
372 systematic upward motion is present (Fig. 4) whatever the longitudinal bin considered. The Hadley
373 cell is further displaced to the South (latitude < 30°N) and its downward branch does not affect
374 significantly the EMB. The tropopause pressure is rather stable from the WMB to the EMB, around
375 260 hPa. The CH_4 distribution shows minimum in the lowermost troposphere and a maximum in
376 the middle troposphere.

377

378 4. CH_4 variability

379 *4.1. CH_4 spatial distribution of the MB*

380 Figure 5 shows the distributions of 1) the CH_4 total columns from IASI over the MB averaged in
381 summer 2009 to compare with the MOCAGE results in time coincidence, and 2) the CH_4 mixing
382 ratios from AIRS at 260 hPa over the MB averaged in summer 2009 to compare with the
383 MOCAGE results at 200 hPa in time coincidence. The measured and modelled data are selected
384 only for the maritime pixels within the boxes [36°N-45°N, 1°E-12°E] and [30°N-37°N, 26°E-37°E]
385 to represent the WMB and the EMB (blue squares in each figure), respectively.

386 Due to its long lifetime (~12 years), CH_4 is considered as a well-mixed species in the
387 troposphere. Nevertheless the CH_4 spatial distribution over the MB in summer (JJA) 2009 shows

388 some gradients both in the East-West and the North-South directions. Indeed, in the middle
389 troposphere (inferred from the sensitivity of the IASI total columns) and in the upper troposphere
390 (200-260 hPa), an East-West gradient is observed in the model and satellite data of ~60 ppbv (~4%)
391 in total column and ~30-150 ppbv (~2-9%) in mixing ratio. A North-South gradient is also detected
392 in the MOCAGE and AIRS data but not in the IASI data set. Therefore, there is systematically a
393 maximum of CH_4 from the middle to the upper troposphere in the East of the MB compared to the
394 West. In the mid-to-upper troposphere, these East-West gradients are not originated from the CH_4
395 sources more intense in Europe than in Northern Africa or in Middle Asia (Fig. 1) but rather from
396 the long-range transport of Asian-origin air masses and the subsidence of air masses in the EMB
397 (Figs. 1-2 and detailed discussion in section 5).

398 Quantitatively, there is a positive bias in MOCAGE vs. IASI of less than 30 ppbv (2%) in CH_4
399 total column mixing ratio. The East-West gradient is rather consistent between IASI and MOCAGE
400 but the North-South modelled gradient is not detected in the IASI data set. In the upper troposphere
401 (200-260 hPa), MOCAGE and AIRS CH_4 mixing ratios are very consistent with gradients more
402 accentuated in the model (~150 ppbv) than in the AIRS data sets (~30 ppbv). A systematic negative
403 bias of MOCAGE compared to AIRS of ~100 ppbv up to 150 ppbv (10%) in the Northern MB is
404 detected. We discuss in the next section the consistency of the vertical profiles of CH_4 as measured
405 by the different spaceborne sensors and as calculated by MOCAGE together with the associated
406 biases.

407

408 *4.2. Vertical profiles*

409 Figure 6 shows the vertical profiles of CH_4 as measured by AIRS (750-100 hPa) and GOSAT
410 (1000-100 hPa) and as calculated by MOCAGE (1000-100 hPa) averaged over the EMB and the
411 WMB depending on the four seasons: winter (DJF), spring (March-April-May, MAM), summer
412 (JJA) and autumn (September-October-November, SON) 2010. There is a good agreement to within
413 20-30 ppbv between AIRS and GOSAT data in the vertical domain 750-200 hPa. GOSAT is

414 systematically greater than AIRS by about 20-30 ppbv for pressure greater than 300 hPa, whilst, for
415 pressure less than 300 hPa, AIRS is systematically greater than GOSAT by 20 ppbv degrading to
416 50-200 ppbv at 100 hPa. But the shape of the vertical spaceborne profiles is consistent between
417 AIRS and GOSAT. Separately, whatever the season considered, the MOCAGE low-to-mid
418 tropospheric CH_4 is low biased compared to the measured profiles by ~150-200 ppbv. Furthermore,
419 the MOCAGE vertical profiles systematically show a maximum at 300 hPa, that is not present in
420 any of the spaceborne measurements, and a strong decrease above.

421 In order to assess the impact of the vertical sensitivity of the spaceborne measurements to the
422 CH_4 profiles, we have applied the AIRS averaging kernels, derived from the AIRS retrieval method
423 (Susskind et al., 2011) and provided by NASA for each AIRS pixel, to the profiles calculated by
424 MOCAGE. Note that the AIRS a priori vertical profiles are not used in our study since we are only
425 interested in the vertical shape of the CH_4 profile and not the absolute amount of CH_4. Degrading
426 the vertical resolution of the MOCAGE profiles by the convolution of averaging kernels (Fig. 6)
427 does show a strong impact on the vertical shape of the CH_4 profiles since the strong maximum at
428 300 hPa is no longer present. Convolved MOCAGE CH_4 profiles are now consistent with AIRS
429 CH_4 profiles whatever the season considered but a systematic low bias of ~150-200 ppbv (8-10%)
430 between AIRS and MOCAGE convolved profiles is observed. This might be due to the fact that no
431 a priori information contributes to the convolved profile. This is also due to the overall
432 underestimation of CH_4 by global models. Indeed, due to coarse horizontal resolution and large
433 uncertainties in the estimated surface emissions, tropospheric CH_4 lifetimes, e.g. evaluated by the
434 multi-model intercomparison project ACCMIP, are about 5-13% lower than observation estimates
435 (Naik et al., 2013; Voulgarakis et al., 2013).

436 Along the vertical, it is almost impossible to validate the spaceborne profiles with an external
437 data set since, even within the Total Carbon Column Observing Network
438 (http://www.tccon.caltech.edu/) giving accurate and precise column-averaged abundances of CH_4
439 (Wunch et al., 2010) because no measurement sites are unfortunately available in the vicinity of the

MB. Near the surface, the amount of CH_4 is about 1700-1750 ppbv for MOCAGE, and is on average less than the CH_4 GOSAT data by about 150-200 ppbv. At this stage, it is worthwhile considering surface data within the MB. The NOAA Earth System Research Laboratory (ESRL) In Situ Methane Measurements provide some surface CH_4 measurements within and/or in the vicinity of the MB: Lampedusa, Italy (35.52°N, 12.62°E, 45 amsl), Centro de Investigacion de la Baja Atmosfera (CIBA), Spain (41.81°N, 4.93°W, 845 amsl) and Negev Desert, Israel (30.86°N, 34.78°E, 477 amsl). On average, these three sites indicate (not shown) a surface CH_4 annual mean of about 1 875 ppbv in 2010, with an annual oscillation of ~20 ppbv amplitude. Consequently, the amount of surface CH_4 in the MOCAGE run for 2010 is actually low biased by about 150-200 ppbv (8-10%) but is very consistent with the LMDz-OR-INCA surface data of ~1725-1750 ppbv over the Mediterranean (Fig. 10). The slight differences between the EMB and the WMB according to the season and height are studied in detail in the next sub-section.

4.3. The East-West seasonal variations: measured and calculated differences

The seasonal variations of the differences in CH_4 fields between the EMB and the WMB (i.e., EMB minus WMB, labelled as "E–W") as measured by AIRS, GOSAT and IASI and as calculated by LMDz-OR-INCA, CNRM-AOCCM and MOCAGE are presented in Figure 7 when considering the upper troposphere (AIRS, GOSAT, LMDz-OR-INCA and CNRM-AOCCM at 260 and 300 hPa) and the middle troposphere (IASI and MOCAGE total column mixing ratios). In the middle and upper troposphere (Fig. 7), despite the fact that spaceborne measurements and modelling of CH_4 are challenging, the modelled and measured seasonal variations of E–W are consistent to each other showing a maximum (peak) in summer and a wide minimum in winter.

If we consider the time evolution of the total column mixing ratios (namely focussing on the middle troposphere), we note that both MOCAGE and IASI show a maximum in summer, although 3 times greater in MOCAGE (~60 ppbv) than in IASI (~20 ppbv) in July and August. The minimum in January-February is close to zero but slightly positive in October (5-10 ppbv). The

much stronger maximum in August calculated by MOCAGE compared to IASI CH_4 total columns might be attributable to the sensitivity of spaceborne measurements in the middle troposphere whilst the MOCAGE tropospheric columns cover the entire troposphere from the surface to the top of the model atmosphere, namely 5 hPa.

In the upper troposphere (300 hPa), the spaceborne instrument datasets show a E–W maximum in summer of ~12 ppbv in August for AIRS and a E–W wide maximum of ~5 ppbv in July-September for GOSAT. A E–W peak of ~10 ppbv in July-August is also calculated by CNRM-AOCCM although, in the LMDz-OR-INCA dataset, the E–W maximum is slightly positive in August (~2 ppbv). The minimum in the satellite datasets is observed in March-April and is negative (from –15 to –20 ppbv) consistently with the LMDz-OR-INCA dataset whilst the CNRM-AOCCM E–W minimum is less intense (–6 ppbv in February and April). The peak-to-peak amplitude of the E–W seasonal variation is almost twice greater in the satellite measurements (~25 ppbv) than in the model data (~15 ppbv). This represents a ~1.5-2.0% variation of CH_4 in the E–W over the entire year. The difference in amplitude between satellite and model in the seasonal evolution of E-W may be due to: a) the comparison technique. There is a broader vertical domain in the measurement data than in the model data; b) regarding the processes in summer, we may have less CH_4 trapped in the Asian Monsoon Anticyclone redistributed towards the EMB (see section 5) in the models compared to the measurements; c) regarding the processes in winter, we may have too much CH_4 transported over the Mediterranean Sea to the East compared to the West, leading to a too smooth E-W gradient in the models compared to the measurements.

We have also to remind that statistically the number of spaceborne measurements used in our analysis (see section 2) is ~5 times greater in IASI compared to AIRS, ~30 times greater in AIRS compared to GOSAT. Consequently, GOSAT monthly-averaged data appear noisier than AIRS monthly-averaged data. Note that IASI total columns are not and cannot be directly compared with AIRS or GOSAT profiles in our analysis. Nevertheless, although IASI data are not operationally produced, the IASI E-W seasonal variation is very consistent with the E-W seasonal variation as

deduced from all other datasets. The monthly random error attributed to the E−W IASI CH_4 is about 0.1%, much less than the observed peak-to-peak yearly variation. We estimate that the AIRS monthly random error attributed to the E−W CH_4 is twice greater than the one calculated for IASI, and that the GOSAT monthly random error is about 5 times greater than the ones calculated for IASI. We discuss in the next section the origin of the summer peak in the E−W seasonal variation.

5. Contribution of the Asian Monsoon Anticyclone

As stated in sections 3 and 4, interpreting the temporal evolution of the E−W CH_4 seasonal evolution along the vertical requires to consider the evolution of CH_4 over the Asian continent because of the importance of long-range transport. From Rodwell and Hoskins (1996), it is known that there is a meteorological link between monsoons and the dynamics of the deserts and more precisely between the Asian monsoon and the EMB summer regime. The subsidence centre over the EMB owes its location, timing of onset and intensity to the Asian monsoon, and not to the Hadley circulation. Although it takes less than one day to reach the upper troposphere within the Asian monsoon, back-trajectory calculation (Ziv et al., 2004) shows that it takes about 3-4 days for an air parcel to reach and descent the upper tropospheric EMB from the vicinity of the anticyclone that develops over the Asian monsoon. Inside the Asian Monsoon Anticyclone (AMA), pollutants like CO originating from the surface constitute about 50% of the CO concentration at 100 hPa (Park et al., 2009), with the reminder resulting from chemical production in the troposphere. Most of the CO within the AMA comes from India and South East Asia, with an insignificant contribution from the Tibetan Plateau. Randel and Park (2006), and Park et al. (2009) have analyzed in detail this phenomenon over Asia by considering dynamical parameters (potential vorticity) and chemical species (H_2O, CO and O_3).

Numerous studies have already evaluated the impact of transport vs. emission of pollutants and aerosols over the MB and its temporal variability considering different pollutants, chemical

517 compounds and aerosols (Wanger et al., 2000; Lelieveld et al., 2002; Pfister et al., 2004; Kallos et
518 al., 2007). As stated in section 3, two main dynamic factors affect the EMB: 1) the upper to mid-
519 tropospheric subsidence, and 2) the lower-level cool Etesian winds (Ziv et al., 2004). Although the
520 EMB is characterized by strong descent in the middle and upper troposphere in summer, transport
521 from the boundary layer accounts for about 25% of the local Middle Eastern contribution to the
522 ozone enhancement in the middle troposphere (Liu et al., 2009). Elevated CO episodes in EMB
523 during summer can also be attributed to synoptic conditions prone to favorable transport from
524 Turkey and Eastern Europe towards the EMB rather than increased emissions (Drori et al., 2012).
525 Upper tropospheric longitudinal gradients in the EMB of CH_4, CO, hydrocarbons, including
526 acetone, methanol, and acetonitrile, halocarbons, O_3 and total reactive nitrogen (NOy) were also
527 attributed in August 2001 to the chemical impact of the Asian plume (Scheeren et al., 2003).
528 Finally, Georgoulias et al. (2011) present some interesting results of CH_4 from space in the vicinity
529 of the Mediterranean Sea, but only over land and essentially over the Eastern Mediterranean. The
530 authors found, from the total columns of CH_4 as measured by SCIAMACHY in 2003 and 2004, an
531 obvious maximum in August that could not be attributed to any volcano eruptions although this
532 area hosts a significant number of geological formations that could potentially contribute to the total
533 CH_4 burden. Being given that the sensitivity of the SCIAMACHY CH_4 total columns covers the
534 vertical domain 1000-200 hPa from the vertical structure of the averaging kernels presented in
535 Buchwitz et al. (2005), we note that 1) this maximum localized in August is consistent with our
536 study, and 2) the impact of the AMA on the CH_4 fields in the mid-to-upper troposphere cannot be
537 ruled out.

538 In order to analyze the climalogical impact of the AMA onto the EMB, we have calculated (Fig.
539 8) the climatological six-day back-trajectories from the point at 33° N, 35° E located in the EMB
540 (red filled circle on Fig. 8) based on the British Atmospheric Data Centre trajectory service
541 (http://badc.nerc.ac.uk/community/trajectory/) from 1st July to 31st August (summer convective
542 period) from 2001 to 2010 every 12 hours at 5 different pressure levels: 850 and 700 hPa (lower

543 troposphere), 500 hPa (middle troposphere), and 300 and 200 hPa (upper troposphere). The position
544 of the gravity centre of each distribution at each level is represented every 24 hours by a star on
545 Figure 8. Data from European Centre for Medium-Range Weather Forecasts (ECMWF) archive (2.5
546 degree/pressure levels) are used in the present calculation. The methodology has been first used
547 over the Dome C (Concordia) station in Antarctica and presented in Ricaud (2014). We have also
548 performed the same analysis but for the winter period from 1st January to 31st March 2001-2010
549 (Fig. 8). Figure 8 undoubtedly shows that air parcels above the EMB during the Asian monsoon
550 period of July-August from 2001 to 2010 are originated: a) from Asia in the upper troposphere, b)
551 from Northern America and Northern Africa in the mid-troposphere and c) from Europe in the low
552 troposphere. The same Figure also shows that in winter (and all other seasons but summer, not
553 shown) air parcels above the EMB are originated from the West (Europe, Atlantic Ocean, North
554 America, Pacific Ocean) whatever the pressure level considered from 850 to 100 hPa.

555 We apply the same climatological approach based on the CNRM-AOCCM and LMDz-OR-
556 INCA CH_4 model results over the period 2001-2010. We consider (Fig. 9) the E–W CH_4 seasonal
557 evolution at pressure levels from the lowermost troposphere to the lowermost stratosphere (850,
558 700, 500, 300, 200 and 100 hPa) and different scenarios for LMDz-OR-INCA (RCPs 2.6, 4.5, 6.0
559 and 8.5) in order to check out whether the summer peak still persists. We also represent the fields of
560 CH_4 as specified and/or calculated in the lowermost level (surface level) by CNRM-AOCCM and
561 by LMDz-OR-INCA (4 scenarios) in summer averaged over the climatological period 2001-2010
562 over a wide area covering the MB and the Asian continent in Figure 10, whilst the CH_4 fields
563 calculated at 200 hPa are shown in Figure 11.

564 The E-W CH_4 seasonal variations from the two models (Fig. 9) behave distinctively in the entire
565 troposphere, and agree very well in the lowermost stratosphere. In the lower troposphere (850 and
566 700 hPa), the E–W CH_4 seasonal evolution from LMDz-OR-INCA exhibits a strong semi-annual
567 oscillation of ±10-15 ppbv peaking in winter and summer for the 4 RCPs whilst the evolution from
568 the CNRM-AOCCM shows a weak annual oscillation of 4-5 ppbv amplitude, with a strong

minimum in summer, namely out-of-phase relative to the LMDz-OR-INCA variation. In the middle troposphere at 500 hPa, the 4 LMDz-OR-INCA outputs exhibit a net maximum in August of ~8 ppbv with minima ranging from –2 to –12 ppbv from October to June, whilst the output from CNRM-AOCCM again shows a strong minimum in summer of about –4 ppbv. At this stage, it is important to remind that the two models are Global Circulation Models (GCMs) with an on-line chemistry. The emissions of CH_4 are time-, longitude- and latitude-dependent in LMDz-OR-INCA with surface maxima over the Northern continent (Fig. 10). In CNRM-AOCCM, there is no emission of CH_4 (Fig. 10) but mixing ratios of CH_4 between the surface and the 560 hPa level are relaxed towards evolving global mean surface abundances. This explains why the two models behave separately for pressures greater or equal to 500 hPa. Note that, regarding the shape of the E–W CH_4 seasonal evolution, there is no significant difference within the different scenarios of the LMDz-OR-INCA outputs since surface CH_4 show the same structures independently of the RCPs considered (Fig. 10).

In the upper troposphere (200 and 300 hPa), the outputs from the two models show a peak in summer in the E–W CH_4 seasonal evolution (Fig. 9), but this differs from the RCPs considered for LMDz-OR-INCA. The maximum is much more intense in CNRM-AOCCM (~8 ppbv in July-August and ~30 ppbv in June-July at 300 and 200 hPa, respectively) than in LMDz-OR-INCA (~1 and ~10 ppbv in August for RCP 4.5 but only –4 and +4 ppbv in August for RCP 8.5 at 300 and 200 hPa, respectively; one peak at –4 ppbv in August for RCP 6.0 at 300 hPa but no peak at 200 hPa; no peak for RCP 2.6 neither at 300 nor at 200 hPa). On average, from 500 to 200 hPa, only the RCP 4.5 scenario from LMDz-OR-INCA shows a positive maximum in summer. At 300 and 200 hPa, the LMDz-OR-INCA summer peak is much less intense than the CNRM-AOCCM summer peak.

It is not obvious to understand why the E-W seasonal variation at 200 hPa is positive in summer for RCP 4.5 and not for the other RCPs (except RCP 8.5 in August). The horizontal distribution of CH_4 calculated by the two models at 200 hPa (Fig. 11) drastically differs but local maxima are

595 centred within the AMA. A zonally-symmetric structure showing a strong South-North gradient in
596 CH_4 is modelled by CNRM-AOCCM with maxima in the tropics (1800 ppbv) and minima at high
597 latitudes (1700 ppbv) and a local maximum centred within the core of the AMA with values greater
598 than 1807 ppbv elongated towards two axis: 1) South-East Asia and 2) Middle East and EMB. The
599 CH_4 field calculated by LMDz-OR-INCA considering the 4 scenarios also shows two maxima over
600 Northern India and over North-East Asia but the horizontal distribution is not zonally-symmetric
601 due to a zonally-asymmetric CH_4 surface field. In all the scenarios considered, the CH_4 maxima
602 within the AMA range from 1710 to 1750 ppbv with increasing RCPs from 2.6 to 8.5. An elongated
603 tongue of enriched CH_4 enters the EMB. More precisely, we can argue that in RCPs 2.6, 6.0 and
604 8.5, the primary maximum of CH_4 is located northward at 50°N, 135°E (CH_4 values greater than
605 1720, 1730 and 1750 ppbv, respectively) although it is a secondary maximum in RCP 4.5 (CH_4
606 values less than 1720 ppbv). Through long-range transport, this mid-latitude maximum is
607 transported Eastward within a band 40°N-50°N enriching CH_4 in the WMB and producing a E-W
608 minimum in summer for RCPs 2.6, 6.0 and 8.5. Since there is a North-South gradient with a
609 maximum in the South for CNRM-AOCCM, CH_4-depleted air masses reach the WMB although
610 CH_4-enriched air masses from the AMA reach the EMB producing a systematic peak in summer,
611 consistently with RCP 4.5.

612 In the lower stratosphere (100 hPa, Fig. 9), all the model outputs are consistent to each other
613 showing an annual oscillation, with a wide maximum in summer (60-80 ppbv) and a wide minimum
614 in winter (20-35 ppbv). This is apparently surprising keeping in mind that both models significantly
615 differ from the surface (see Fig. 10) to ~500 hPa. But, in the WMB, the 100-hPa pressure
616 corresponds to 420-K potential temperature both in summer (Fig. 2) and in winter (Fig. 4) whilst, in
617 the EMB, it corresponds to 390 K in summer and 400 K in winter, namely closer to the tropopause
618 in summer than in winter. Consequently, whatever the model considered, the E-W CH_4 seasonal
619 variation at 100 hPa a) is always positive and b) shows a peak in the summer period. We note that
620 the summer peak in E–W seasonal evolution from the middle to the upper troposphere has also been

observed and calculated by considering other constituents like CO and O_3 (not shown). This is the main topic of a forthcoming paper.

In conclusion, a schematic representation of the summertime processes impacting mid-to-upper CH_4 in the EMB is presented in Figure 12. In our study, whatever the amount of CH_4 at the surface and its horizontal distribution, 1850-2000 ppbv for LMDz-OR-INCA consistently with the emission sources (Asia, Northern and Eastern Europe, Central Africa) or 1820 ppbv uniformly spread (Fig. 10), the Asian monsoon traps elevated amounts of CH_4 that converge through the depression, and are uplifted up to the upper troposphere at 200 hPa (Fig. 11) where they build up. At this level, the AMA re-distributes elevated amounts of CH_4 towards Middle East, North Africa and the EMB through long-range transport. Finally, elevated amounts of CH_4 build up in the EMB where they descend to the middle troposphere.

6. Conclusions

The present study is part of the Chemical and Aerosol Mediterranean Experiment (ChArMEx) programme. The aim is to investigate the tropospheric CH_4 time and space variations above the Mediterranean Basin (MB) and to attribute the variability to differing synoptic and global scales depending on the season and the altitude layer considered. Since the analysis of the mid-to-upper tropospheric CH_4 distribution from spaceborne sensors and model outputs is challenging, we have used a wide variety of datasets. 1) The spaceborne measurements from Thermal Infrared (TIR) instruments: Thermal And Near infrared Sensor for carbon Observations - Fourier Transform Spectrometer (TANSO-FTS) instrument on the Greenhouse gases Observing SATellite (GOSAT) satellite, the Atmospheric InfraRed Spectrometer (AIRS) on the Aura platform and the Infrared Atmospheric Sounder Interferometer (IASI) instrument aboard the MetOp-A platform. 2) The model results from the Chemical Transport Model (CTM) MOCAGE, and the two Chemical Climate Models (CCMs) CNRM-AOCCM and LMDz-OR-INCA (the later considering different emission scenarios, RCPs 2.6, 4.5, 6.0 and 8.5).

Since CH_4 is a long-lived tracer with lifetime of ~12 years and is supposed to be well mixed in the troposphere, we had to adopt a climatological approach to highlight the weak expected variability. Spaceborne measurements and the model results were selected and monthly-averaged only over the Mediterranean Sea. The period under interest spans from 2008 to 2011 for the satellite measurements and the MOCAGE model results whilst, regarding the CCMs, we have averaged the model outputs over the climatological period from 2001 to 2010.

From both satellite and model results, our study obviously demonstrates the persistence of an East-West gradient in CH_4 from the middle to the upper troposphere with a maximum in the Western MB whatever the season considered except in summer when larger amounts of CH_4 accumulate above the Eastern MB. In winter, air masses mainly originating from Atlantic Ocean and Europe tend to favour an elevated amount of mid-to-upper tropospheric CH_4 in the West compared to the East of the MB, with a general upward transport above the MB. In summer, the meteorological condition of the MB is changed, favouring air from Northern Africa and Middle East together with Atlantic Ocean and Europe, with a general descent above the Eastern MB.

Our analysis shows that, in the upper troposphere (300 hPa), the peak-to-peak amplitude of the East–West seasonal variation in CH_4 above the MB is weak but almost twice greater in the satellite measurements (~25 ppbv) than in the model data (~15 ppbv).. The maximum of CH_4 in summer above the Eastern MB can be explained by a series of dynamical processes only occurring in summer. The Asian monsoon traps and uplifts high amounts of CH_4 to the upper troposphere where they build up. The Asia monsoon Anticyclone redistributes these elevated CH_4 amounts towards North Africa and Middle East to finally reach and descent in the Eastern MB. Consequently, the seasonal variation of the difference in CH_4 between the East and the West MB shows a maximum in summer for pressures from 500 to 100 hPa considering both spaceborne measurements and model results whatever the emission scenarios used for the CCMs. But only the RCP 4.5 scenario gives systematically a positive summer peak whatever the pressure level considered, consistently with the measurements.

From this study, we conclude that CH_4 in the mid-to-upper troposphere over the MB is mainly affected by long-range transport, particularly intense in summer from Asia. Conversely, in the lower troposphere, the CH_4 variability is driven by the local sources of emission in the vicinity of the MB. Other constituents can also be affected by this summer mechanism e.g. O_3 and CO (not shown). In a forthcoming paper, the time evolution of the CH_4, O_3 and CO fields above the MB and at the Asian scale is being studied by considering the outputs from different CCMs in the contemporary period (2000-2010) in order to study the future evolution of the chemical climate over the MB by 2100. Finally, despite the fact that IASI CH_4 data as delivered by EUMETSAT are not operational, the seasonal variation of the East-West difference in CH_4 total columns is nevertheless consistent with theoretical results and measurements from AIRS and IASI.

Acknowledgments. We would like to thank the following institutes and programme for funding our study: Centre National de la Recherche Scientifique-Institut National des Sciences de l'Univers/CNRS-INSU, Centre National des Etudes Spatiales/CNES, Agence de l'Environnement et de la Maîtrise del'Energie/ADEME through the programme the Mediterranean Integrated STudies at Regional And Local Scales/MISTRALS Chemistry-Aerosol Mediterranean Experiment/ChArMEx. We also thank the following data bases for accessing the data: the French database Ether, the European Organisation for the Exploitation of Meteorological Satellites, the GOSAT User Interface Gateway, the National Oceanic and Atmospheric Administration, the British Atmospheric Data Centre to access the LMDz-OR-INCA model data through the international Atmospheric Chemistry and Climate Model Intercomparison Project initiative, and the Global Atmosphere Watch from the World Meteorological Organization. Thanks to the British Atmospheric Data Centre, which is part of the Natural Environment Research Council (NERC) National Centre for Atmospheric Science (NCAS), for the calculation of trajectories and access to European Centre for Medium-Range Weather Forecasts (ECMWF) data.

698 **References**

699 August, T., Klaes, D., Schlüssel, P., Hultberg, T., Crapeau, M., Arriaga, A., O'Carroll, A., Coppens,
700 D., Munro, R., and Calbet, X.: IASI on Metop-A: Operational Level 2 retrievals after five years
701 in orbit, J. Quant. Spectrosc. Rad. Transfer, 113:11, 1340-1371, 2012.

702 Bergamaschi, P., Frankenberg, C., Fokke Meirink, J., Krol, M., Villani, M. G., Houweling, S.,
703 Dentener, F., Dlugokencky, E. J., Miller, J. B., Gatti, L. V., Engel, A., and Levin, I.: Inverse
704 modeling of global and regional CH4 emissions using SCIAMACHY satellite retrievals, J.
705 Geophys. Res., 114, D22301, doi:10.1029/2009JD012287, 2009.

706 Bousquet, P., Ringeval, B., Pison, I., Dlugokencky, E. J., Brunke, E.-G., Carouge, C., Chevallier,
707 F., Fortems-Cheiney, A., Frankenberg, C., Hauglustaine, D. A., Krummel, P. B., Langenfelds, R.
708 L., Ramonet, M., Schmidt, M., Steele, L. P., Szopa, S., Yver, C., Viovy, N., and Ciais, P.: Source
709 attribution of the changes in atmospheric methane for 2006–2008, Atmos. Chem. Phys., 11,
710 3689-3700, doi:10.5194/acp-11-3689-2011, 2011.

711 Buchwitz, M., Rozanov, V. V., and Burrows, J. P.: A near-infrared optimized DOAS method for
712 the fast global retrieval of atmospheric CH4, CO, CO2, H2O, and N2O total column amounts
713 from SCIAMACHY Envisat-1 nadir radiances, J. Geophys. Res., 105(D12), 15231–15245,
714 doi:10.1029/2000JD900191, 2000.

715 Buchwitz, M., de Beek, R., Burrows, J. P., Bovensmann, H., Warneke, T., Notholt, J., Meirink, J.
716 F., Goede, A. P. H., Bergamaschi, P., Körner, S., Heimann, M., and Schulz, A.: Atmospheric
717 methane and carbon dioxide from SCIAMACHY satellite data: initial comparison with
718 chemistry and transport models, Atmos. Chem. Phys., 5, 941-962, doi:10.5194/acp-5-941-2005,
719 2005.

720 Claeyman, M., Attié, J.-L., El Amraoui, L., Cariolle, D., Peuch, V.-H., Teyssèdre, H., Josse, B.,
721 Ricaud, P., Massart, S., Piacentini, A., Cammas, J.-P., Livesey, N. J., Pumphrey, H. C., and
722 Edwards, D. P.: A linear CO chemistry parameterization in chemistry-transport models:
723 evaluation and application to data assimilation, Atmos. Chem. Phys., 10, 6097-6115, 2010.

724 Claeyman, M., Attié, J.-L., Peuch, V.-H., El Amraoui, L., Lahoz, W. A., Josse, B., Ricaud, P., von
725 Clarmann, T., Höpfner, M., Orphal, J., Flaud, J.-M., Edwards, D. P., Chance, K., Liu, X.,
726 Pasternak, F., and Cantié, R.: A geostationary thermal infrared sensor to monitor the lowermost
727 troposphere: O_3 and CO retrieval studies, Atmos. Meas. Tech., 4, 297-317, 2011.
728 Clerbaux, C., Chazette, P., Hadji-Lazaro, J., Mégie, G., Müller, J.-F., and Clough, S. A.: Remote
729 sensing of CO, CH4, and O3 using a spaceborne nadir-viewing interferometer, J. Geophys. Res.,
730 103, 18999–19013, doi:10.1029/98JD01422, 1998.
731 Courtier, P., Freydier, C., Geleyn, J. F., Rabier, F., and Rochas, M.: The ARPEGE project at
732 METEO-FRANCE. In: Proc ECMWF Workshop. Numerical methods in atmospheric modelling,
733 9–13 Sept 1991, 2, 193–231. ECMWF, Shinfield Park, Reading, UK, 1991.
734 Crevoisier, C., Nobileau, D., Armante, R., Crépeau, L., Machida, T., Sawa, Y., Matsueda, H.,
735 Schuck, T., Thonat, T., Pernin, J., Scott, N. A., and Chédin, A.: The 2007–2011 evolution of
736 tropical methane in the mid-troposphere as seen from space by MetOp-A/IASI, Atmos. Chem.
737 Phys., 13, 4279-4289, doi:10.5194/acp-13-4279-2013, 2013.
738 Cros, B., Durand, P., and Cachier, H.: An overview of the ESCOMPTE campaign, Atmos. Res,
739 69(3-4), 241-279, 2004.
740 Dayan, U.: Climatology of Back Trajectories from Israel Based on Synoptic Analysis. J. Climate
741 Appl. Meteor., 25, 591–595. doi: http://dx.doi.org/10.1175/1520-0450(1986), 1986.
742 Dentener, F., Stevenson, D., Cofala, J., Mechler, R., Amann, M., Bergamaschi, P., Raes, F., and
743 Derwent, R.: The impact of air pollutant and methane emission controls on tropospheric ozone
744 and radiative forcing: CTM calculations for the period 1990–2030, Atmos. Chem. Phys., 5,
745 1731–1755, http://www.atmos-chem-phys.net/5/1731/2005/, 2005.
746 Drori, R., Dayan, U., Edwards, D. P., Emmons, L. K., and Erlick, C.: Attributing and quantifying
747 carbon monoxide sources affecting the Eastern Mediterranean: a combined satellite, modelling,
748 and synoptic analysis study, Atmos. Chem. Phys., 12, 1067-1082, doi:10.5194/acp-12-1067-
749 2012, 2012.

750 Dufour, A., Amodei, M., Ancellet, G., and Peuch, V.-H.: Observed and modelled “chemical
751 weather” during ESCOMPTE, Atmos. Res., 74, 161–189, 2005.
752 El Amraoui, L., Attié, J.-L., Semane, N., Claeyman, M., Peuch, V.-H., Warner, J., Ricaud, P.,
753 Cammas, J.-P., Piacentini, A., Cariolle, D., Massart, S., and Bencherif, H.: Midlatitude
754 stratosphere – troposphere exchange as diagnosed by MLS O3 and MOPITT CO assimilated
755 fields, Atmos. Chem. Phys., 10, 2175-2194, 2010.
756 EUMETSAT, IASI Level 2 Products Guide, EUM/OPS-EPS/MAN/04/0033. Available on
757 http://oiswww.eumetsat.org/WEBOPS/eps-pg/IASI-L2/IASIL2-PG-0TOC.htm, 2004.
758 Folberth, G. A., Hauglustaine, D. A., Lathière, J., and Brocheton, F.: Interactive chemistry in the
759 Laboratoire de Météorologie Dynamique general circulation model: model description and
760 impact analysis of biogenic hydrocarbons on tropospheric chemistry, Atmos. Chem. Phys.,
761 6:2273–2319. www.atmos-chem-phys.net/6/2273/2006/, 2006.
762 Georgoulias, A. K., Kourtidis, K. A., Buchwitz, M., Schneising, O., and Burrows, J. P.: A case
763 study on the application of SCIAMACHY satellite methane measurements for regional studies:
764 the Greater Area of Eastern Mediterranean, Int. J. Remote Sens., 32(3), 787-813,
765 doi:10.1080/01431161.2010.517791, 2011.
766 Giorgi, F., and Lionello, P.: Climate change projections for the Mediterranean region, Global and
767 Planetary Change, 63(2), 90–104, doi:10.1016/j.gloplacha.2007.09.005, 2008.
768 Hauglustaine, D. A., Hourdin, F., Jourdain, L., Filiberti, M.-A., Walters, S., Lamarque, J.-F., and
769 Holland, E. A.: Interactive chemistry in the Laboratoire de Meteorologie Dynamique general
770 circulation model: description and background tropospheric chemistry evaluation, J. Geophys.
771 Res., 109:D04314. doi:10.1029/2003JD003957, 2004.
772 Hilton, F., Armante, R., August, T., Barnet, C., Bouchard, A., Camy-Peyret, C., Capelle, V.,
773 Clarisse, L., Clerbaux, C., Coheur, P.-F., Collard, A., Crevoisier, C., Dufour, G., Edwards, D.,
774 Faijan, F., Fourrié, N., Gambacorta, A., Goldberg, M., Guidard, V., Hurtmans, D., Illingworth,
775 S., Jacquinet-Husson, N., Kerzenmacher, T., Klaes, D., Lavanant, L., Masiello, G., Matricardi,

776 M., McNally, A., Newman, S., Pavelin, E., Payan, S., Péquignot, E., Peyridieu, S., Phulpin, T.,
777 Remedios, J., Schlüssel, P., Serio, C., Strow, L., Stubenrauch, C., Taylor, J., Tobin, D., Wolf,
778 W., and Zhou, D.: Hyperspectral Earth Observation from IASI: Five Years of Accomplishments,
779 B. Am. Meteor. Soc., 93, 347–370, doi:10.1175/BAMS-D-11-00027.1, 2012.
780 Hourdin, F., Musat, I., Bony, S., Braconnot, P., Codron, F., Dufresne, J.-L., Fairhead, L., Filiberti,
781 M.-A., Friedlingstein, P., Grandpeix, J.-Y., Krinner, G., LeVan, P., Li, Z.-X., and Lott, F.: The
782 LMDZ4 general circulation model: climate performance and sensitivity to parametrized physics
783 with emphasis on tropical convection, Clim. Dyn., 27, 787–813, doi:10.1007/s00382-006-0158-
784 0, 2006.
785 Huszar, P., Teyssèdre, H., Cariolle, D., Olivié, D. J. L., Michou, M., Saint-Martin, D., Senesi, S.,
786 Voldoire, A., Salas y Melia, D., Alias, A., Karcher, F., Ricaud, P., and Halenka, T.: Modeling
787 the present and future impact of aviation on climate: an AOGCM approach with online coupled
788 chemistry, Atmos. Chem. Phys., 13, 10027-10048, doi:10.5194/acp-13-10027-2013, 2013.
789 Imasu, R., Saitoh, N., and Niwa, Y.: Retrieval performance of GOSAT thermal infrared FTS sensor
790 for measuring CO_2 concentrations, Proc. SPIE 6744, Sensors, Systems, and Next-Generation
791 Satellites XI, 67440F, http://dx.doi.org/10.1117/12.737796, 2007.
792 IPCC: Climate change 2007: The physical science basis. Contribution of working group I to the
793 fourth assessment report of the intergovernmental panel on climate change, Cambridge, UK and
794 New York, USA, Cambridge University Press, 996 pp., 2007.
795 Josse, B., Simon, P., and Peuch, V.-H.: Rn−222 global simulations with the multiscale CTM
796 MOCAGE, Tellus, 56B, 339–356, 2004.
797 Kallos, G., Astitha, M., Katsafados, P., and Spyrou, C.: Long-Range Transport of
798 Anthropogenically and Naturally Produced Particulate Matter in the Mediterranean and North
799 Atlantic: Current State of Knowledge, J. Appl. Meteorol. Clim., 46, 1230-1251, 2007.
800 Krinner, G., Viovy, N., de Noblet-Ducoudré, N., Ogée, J., Polcher, J., Friedlingstein, P., Ciais, P.,
801 Sitch, S., and Prentice, I. C.: A dynamic global vegetation model for studies of the coupled

802 atmosphere-biosphere system, Global Biogeochem. Cycles, 19, GB1015,
803 doi:10.1029/2003GB002199, 2005.
804 Kuze, A., Suto, H., Nakajima, M., and Hamazaki, T.: Thermal and near infrared sensor for carbon
805 observation Fourier-transform spectrometer on the Greenhouse Gases Observing Satellite for
806 greenhouse gases monitoring, Appl. Opt., 48, 6716-6733, 2009.
807 Ladstätter-Weißenmayer, A., Heland, J., Kormann, R., von Kuhlmann, R., Lawrence, M. G.,
808 Meyer-Arnek, J., Richter, A., Wittrock, F., Ziereis, H., and Burrows, J.-P.: Transport and build-
809 up of tropospheric trace gases during the MINOS campaign: comparison of GOME, in situ
810 aircraft measurements and MATCH-MPIC-data, Atmos. Chem. Phys., 3, 1887–1902, 2003.
811 Lamarque, J.-F., Kyle, G. P., Meinshausen, M., Riahi, K., Smith, S. J., van Vuuren, D. P., Conley,
812 A. J., and Vitt, F.: Global and regional evolution of short-lived radiatively-active gases and
813 aerosols in the Representative Concentration Pathways, Climatic Change, 109:191–212 DOI
814 10.1007/s10584-011-0155-0, 2011.
815 Lamarque, J.-F., Shindell, D. T., Josse, B., Young, P. J., Cionni, I., Eyring, V., Bergmann, D.,
816 Cameron-Smith, P., Collins, W. J., Doherty, R., Dalsoren, S., Faluvegi, G., Folberth, G., Ghan,
817 S. J., Horowitz, L. W., Lee, Y. H., MacKenzie, I. A., Nagashima, T., Naik, V., Plummer, D.,
818 Righi, M., Rumbold, S. T., Schulz, M., Skeie, R. B., Stevenson, D. S., Strode, S., Sudo, K.,
819 Szopa, S., Voulgarakis, A., and Zeng, G.: The Atmospheric Chemistry and Climate Model
820 Intercomparison Project (ACCMIP): overview and description of models, simulations and
821 climate diagnostics, Geosci. Model Dev., 6, 179-206, 2013.
822 Lefèvre, F., Brasseur, G. P., Folkins, I., Smith, A. K., and Simon, P.: Chemistry of the 1991–1992
823 stratospheric winter: Three-dimensional model simulations, J. Geophys. Res., 99, 9183–8195,
824 1994.
825 Lelieveld, J., Berresheim, H., Borrmann, S., Crutzen, P. J., Dentener, F. J., Fischer, H., Feichter, J.,
826 Flatau, P. J., Heland, J., Holzinger, R., Korrmann, R., Lawrence, M. G., Levin, Z., Markowicz,

827 K. M., Mihalopoulos, N., Minikin, A., Ramanathan, V., de Reus, M., Roelofs, G. J., Scheeren,
828 H. A., Sciare, J., Schlager, H., Schultz, M., Siegmund, P., Steil, B., Stephanou, E. G., Stier, P.,
829 Traub, M., Warneke, C., Williams, J., and Ziereis, H.: Global Air Pollution Crossroads over the
830 Mediterranean, Science, 298, 5594, 794-799, DOI: 10.1126/science.1075457, 2002.

831 Lionello, P. (Ed.): The Climate of the Mediterranean Region: From the past to the future. 592p,
832 Elsevier, 2012.

833 Liu, J. J., Jones, D. B. A., Worden, J. R., Noone, D., Parrington, M., and Kar, J.: Analysis of the
834 summertime buildup of tropospheric ozone abundances over the Middle East and North Africa
835 as observed by the Tropospheric Emission Spectrometer instrument, J. Geophys. Res., 114,
836 D05304, doi:10.1029/2008JD010993, 2009.

837 Masson, O., Piga, D., Gurriaran, R., and D'Amico, D.: Impact of an exceptional Saharan dust
838 outbreak in France: PM10 and artificial radionuclides concentrations in air and in dust deposit,
839 Atmos. Env., 44, 20, 2478–2486, http://dx.doi.org/10.1016/j.atmosenv.2010.03.004, 2010.

840 Michou, M., and Peuch, V.-H.: Surface exchanges in the MOCAGE multiscale Chemistry and
841 Transport Model, J. Water Sci., 15, 173–203, 2002.

842 Michou, M., Saint-Martin, D., Teyssèdre, H., Alias, A., Karcher, F., Olivié, D., Voldoire, A., Josse,
843 B., Peuch, V.-H., Clark, H., Lee, J. N., and Cheroux, F.: A new version of the CNRM
844 Chemistry-Climate Model, CNRM-CCM: description and improvements from the CCMVal-2
845 simulations, Geosci. Model Dev., 4, 873–900, doi:10.5194/gmd-4-873-2011, 2011.

846 Millán, M. M., Salvador, R., Mantilla, E., and Kallos, G.: Photooxidant dynamics in the
847 Mediterranean basin in summer: Results from European research projects, J. Geophys. Res., 102,
848 8811–8823, doi:10.1029/96JD03610, 1997.

849 Nabat, P., Solmon, F., Mallet, M., Kok, J. F., and Somot, S.: Dust emission size distribution impact
850 on aerosol budget and radiative forcing over the Mediterranean region: a regional climate model
851 approach, Atmos. Chem. Phys., 12, 10545-10567, 2012.

852 Naik, V., Voulgarakis, A., Fiore, A. M., Horowitz, L. W., Lamarque, J.-F., Lin, M., Prather, M. J.,
853 Young, P. J., Bergmann, D., Cameron-Smith, P. J., Cionni, I., Collins, W. J., Dalsøren, S. B.,
854 Doherty, R., Eyring, V., Faluvegi, G., Folberth, G. A., Josse, B., Lee, Y. H., MacKenzie, I. A.,
855 Nagashima, T., van Noije, T. P. C., Plummer, D. A., Righi, M., Rumbold, S. T., Skeie, R.,
856 Shindell, D. T., Stevenson, D. S., Strode, S., Sudo, K., Szopa, S., and Zeng, G.: Preindustrial to
857 present-day changes in tropospheric hydroxyl radical and methane lifetime from the
858 Atmospheric Chemistry and Climate Model Intercomparison Project (ACCMIP), Atmos. Chem.
859 Phys., 13, 5277-5298, doi:10.5194/acp-13-5277-2013, 2013.
860 Park, M., Randel, W. J., Emmons, L. K., and Livesey, N. J.: Transport pathways of carbon
861 monoxide in the Asian summer monsoon diagnosed from Model of Ozone and Related Tracers
862 (MOZART), J. Geophys. Res., 114, D08303, doi:10.1029/2008JD010621, 2009.
863 Peuch, V.-H., Amodei, M., Barthet, T., Cathala, M.-L., Josse, B., Michou, M., and Simon, P. :
864 MOCAGE: Modèle de Chimie, Atmosphérique A Grande Echelle, Actes des Atelier de
865 Modélisation de l'Atmosphère, Météo-France, 33–36, 1999.
866 Pfister, G., Petron, G., Emmons, L. K., Gille, J. C., Edwards, D. P., Lamarque, J.-F., J.-L. Attié, C.
867 Granier, and Novelli, P. C: Evaluation of CO simulations and the analysis of the CO budget for
868 Europe, J. Geophys. Res.-Atmos. (1984–2012), 109(D19), 2004.
869 Randel, W. J., and Park, M.: Deep convective influence on the Asian summer monsoon anticyclone
870 and associated tracer variability observed with Atmospheric Infrared Sounder (AIRS), J.
871 Geophys. Res., 111, D12314, doi:10.1029/2005JD006490, 2006.
872 Razavi, A., Clerbaux, C., Wespes, C., Clarisse, L., Hurtmans, D., Payan, S., Camy-Peyret, C., and
873 Coheur, P. F.: Characterization of methane retrievals from the IASI space-borne sounder, Atmos.
874 Chem. Phys., 9, 7889–7899, 2009.
875 Ricaud, P., Attié, J.-L., Teyssèdre, H., El Amraoui, L., Peuch, V.-H., Matricardi, M., and
876 Schluessel, P.: Equatorial total column of nitrous oxide as measured by IASI on MetOp-A:

implications for transport processes, Atmos. Chem. Phys., 9, 3947-3956, doi:10.5194/acp-9-3947-2009, 2009.

Ricaud, P.: Variabilités de la vapeur d'eau et de la température troposphérique mesurées par le radiomètre micro-onde HAMSTRAD au Dôme C, Antarctique. Partie II : Résultats scientifiques, La Météorologie, 85, 35-46, doi: 10.4267/2042/53749, 2014.

Rodgers, C. D., *Inverse Methods for Atmospheric Sounding: Theory and Practice*, 1st ed. Singapore: World Scientific, 2000.

Rodwell, M. J., and Hoskins, B. J.: Monsoons and the dynamics of deserts, Q. J. R. Meteorol. Soc., 122, 1385-1404, 1996.

Saitoh, N., Touno, M., Hayashida, S., Imasu, R., Shiomi, K., Yokota, T., Yoshida, Y., Machida, T., Matsueda, H., and Sawa, Y.: Comparisons between XCH_4 from GOSAT Shortwave and Thermal Infrared Spectra and Aircraft CH_4 Measurements over Guam, SOLA, 8, 145−149, doi:10.2151/sola.2012-036, 2012.

Scheeren, H. A., Lelieveld, J., Roelofs, G. J., Williams, J., Fischer, H., de Reus, M., de Gouw, J. A., Bolder, M., van der Veen, C., and Lawrence, M.: The impact of monsoon outflow from India and Southeast Asia in the upper troposphere over the eastern Mediterranean, Atmos. Chem. Phys., 3, 1589–1608, 2003.

Schicker, I., Radanovics, S., and Seibert, P.: Origin and transport of Mediterranean moisture and air, Atmos. Chem. Phys., 10, 5089-5105, doi:10.5194/acp-10-5089-2010, 2010.

Scheeren, H. A., Lelieveld, J., Roelofs, G. J., Williams, J., Fischer, H., de Reus, M., de Gouw, J. A., Warneke, C., Holzinger, R., Schlager, H., Klüpfel, T., Bolder, M., van der Veen, C., and Lawrence, M.: The impact of monsoon outflow from India and Southeast Asia in the upper troposphere over the eastern Mediterranean, Atmos. Chem. Phys., 3, 1589-1608, doi:10.5194/acp-3-1589-2003, 2003.

Schlüssel, P., Hultberg, T. H., Phillips, P. L., August, T., and Calbet, X.: The operational IASI Level 2 Processor, Adv. Space Res., 36, 982-988, 2005.

Stockwell, W. R., Kirchner, F., Kuhn, M., and Seefeld, S.: A new mechanism for regional atmospheric chemistry modelling, J. Geophys. Res.: Atmospheres (1984–2012), 102(D22), 25847-25879, 1997.

Susskind, J., Blaisdell, J. M., Iredell, L. and Keita, F.: Improved Temperature Sounding and Quality Control Methodology Using AIRS/AMSU Data: The AIRS Science Team Version 5 Retrieval Algorithm, IEEE Trans. Geosc. Remote Sens., 49, 883-907, 2011.

Szopa, S., Balkanski, Y., Schulz, M., Bekki, S., Cugnet, D., Fortems-Cheiney, A., Turquety, S., Cozic, A., Déandreis, C., Hauglustaine, D., Idelkadi, A., Lathière, J., Lefèvre, F., Marchand, M., Vuolo, R., Yan, N., and Dufresne, J.-L.: Aerosol and ozone changes as forcing for climate evolution between 1850 and 2100, Clim. Dynam., 40, 2223-2250, 2013. DOI:10.1007/s00382-012-1408-y

Turquety, S., Hadji-Lazaro, J., Clerbaux, C., Hauglustaine, D. A., Clough, S. A., Cassé, V., Schlüssel, P., and Mégie, G.: Operational trace gas retrieval algorithm for the Infrared Atmospheric Sounding Interferometer, J. Geophys. Res., 109, D21301, doi:10.1029/2004JD004821, 2004.

van der Werf, G. R., Randerson, J. T., Collatz, G. J., and Giglio, L.: Carbon emissions from fires in tropical and subtropical ecosystems, Global Change Biol., 9, 547–562, 2003.

Voldoire, A., Sanchez-Gomez, E., Salas y Melia, D., Decharme, B., Cassou, C., Sénési, S., Valcke, S., Beau, I., Alias, A., Chevallier, M., Deque, M., Deshayes, J., Douville, H., Fernandez, E., Madec, G., Maisonnave, E., Moine, M.-P., Planton, S., Saint-Martin, D., Szopa, S., Tyteca, S., Alkama, R., Belamari, S., Braun, A., Coquart, L., and Chauvin, F.: The CNRM-CM5.1 global climate model: description and basic evaluation, Clim. Dynam., doi:10.1007/s00382-011-1259-y, 2012.

Voulgarakis, A., Naik, V., Lamarque, J.-F., Shindell, D. T., Young, P. J., Prather, M. J., Wild, O., Field, R. D., Bergmann, D., Cameron-Smith, P., Cionni, I., Collins, W. J., Dalsøren, S. B., Doherty, R. M., Eyring, V., Faluvegi, G., Folberth, G. A., Horowitz, L. W., Josse, B.,

MacKenzie, I. A., Nagashima, T., Plummer, D. A., Righi, M., Rumbold, S. T., Stevenson, D. S., Strode, S. A., Sudo, K., Szopa, S., and Zeng, G.: Analysis of present day and future OH and methane lifetime in the ACCMIP simulations, Atmos. Chem. Phys., 13, 2563-2587, doi:10.5194/acp-13-2563-2013, 2013.

Wanger, A., Peleg, M., Sharf, G., Mahrer, Y., Dayan, U., Kallos, G., Kotroni, V., Lagouvardos, K., Varinou, M., Papadopoulos, A., and Luria, M.: Some Observational and Modelling Evidence of Long Range Transport of Air Pollutants from Europe Towards the Israeli Coast, J. Geophys. Res., 105, 7177-7186, 2000.

Worden, J., Kulawik, S., Frankenberg, C., Payne, V., Bowman, K., Cady-Peirara, K., Wecht, K., Lee, J. E., and Noone, D.: Profiles of CH4, HDO, H2O, and N2O with improved lower tropospheric vertical resolution from Aura TES radiances, Atmos. Meas. Tech., 5, 397–411, www.atmos-meas-tech.net/5/397/2012/doi:10.5194/amt-5-397-2012, 2012.

Wunch, D., Toon, G. C., Wennberg, P. O., Wofsy, S. C., Stephens, B. B., Fischer, M. L., Uchino, O., Abshire, J. B., Bernath, P., Biraud, S. C., Blavier, J.-F. L., Boone, C., Bowman, K. P., Browell, E. V., Campos, T., Connor, B. J., Daube, B. C., Deutscher, N. M., Diao, M., Elkins, J. W., Gerbig, C., Gottlieb, E., Griffith, D. W. T., Hurst, D. F., Jiménez, R., Keppel-Aleks, G., Kort, E. A., Macatangay, R., Machida, T., Matsueda, H., Moore, F., Morino, I., Park, S., Robinson, J., Roehl, C. M., Sawa, Y., Sherlock, V., Sweeney, C., Tanaka, T., and Zondlo, M. A.: Calibration of the Total Carbon Column Observing Network using aircraft profile data, Atmos. Meas. Tech., 3, 1351-1362, doi:10.5194/amt-3-1351-2010, 2010.

Xiong, X., Barnet, C., Maddy, E., Sweeney, C., Liu, X., Zhou, L., and Goldberg, M.: Characterization and validation of methane products from the Atmospheric Infrared Sounder (AIRS), J. Geophys. Res., 113, G00A01, doi:10.1029/2007JG000500., 2008.

Yokota, T., Yoshida, Y., Eguchi, N., Ota, Y., Tanaka, T., Watanabe, H., and Maksyutov, S.: Global Concentrations of CO2 and CH4 Retrieved from GOSAT: First Preliminary Results, SOLA, 5, 160-163, doi:10.2151/sola.2009, 2009.

955 Yoshida, Y., Kikuchi, N., Morino, I., Uchino, O., Oshchepkov, S., Bril, A., Saeki, T., Schutgens,
956 N., Toon, G. C., Wunch, D., Roehl, C. M., Wennberg, P. O., Griffith, D. W. T., Deutscher, N.
957 M., Warneke, T., Notholt, J., Robinson, J., Sherlock, V., Connor, B., Rettinger, M., Sussmann,
958 R., Ahonen, P., Heikkinen, P., Kyrö, E., Mendonca, J., Strong, K., Hase, F., Dohe, S., and
959 Yokota, T.: Improvement of the retrieval algorithm for GOSAT SWIR XCO2 and XCH4 and
960 their validation using TCCON data, Atmos. Meas. Tech., 6, 1533-1547, doi:10.5194/amt-6-
961 1533-2013, 2013.
962 Ziv, B., Saaroni, H., and Alpert, P.: The factors governing the summer regime of the eastern
963 Mediterranean, Int. J. Climatol., 24, 1859–1871, doi: 10.1002/joc.1113, 2004.
964

964 **Table 1.** Nadir-viewing instruments having the capabilities to measure CH_4 in the troposphere.
965 Please, refer to the text for the acronyms.
966

Platform	**Instrument**	**Operation time**	**Wavelength**
ADEOS-1	IMG	1996-1997	TIR
ENVISAT	SCIAMACHY	2002-2012	NIR
Aura	TES	2004-date	TIR
GOSAT	TANSO-FTS	2008-date	SWIR & TIR
Aqua	AIRS	2004-date	TIR
MetOp-A	IASI	2008-date	TIR
MetOp-B	IASI	2012-date	TIR
MetOp-C	IASI	Expected in 2016	TIR

967
968
969

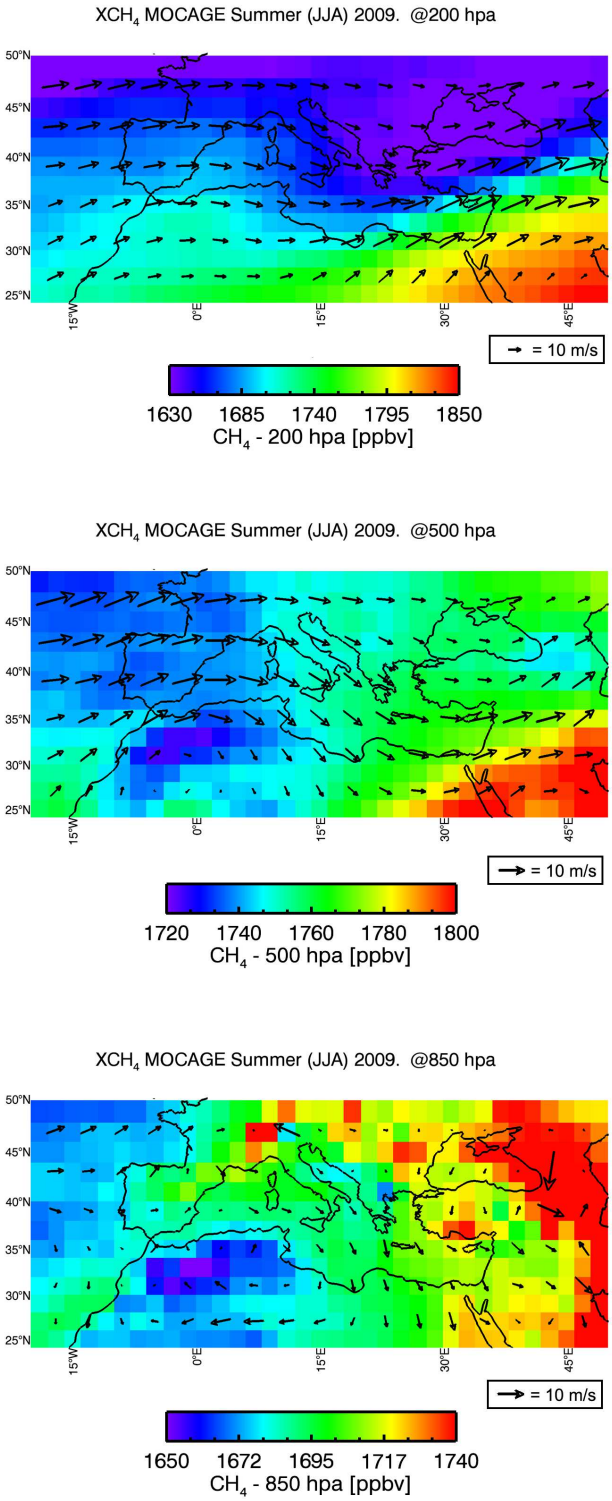

969

970 **Figure 1.** (From bottom to top) Fields of CH_4 as calculated by MOCAGE and averaged for summer
971 (JJA) 2009 at 850, 500 and 200 hPa. Superimposed are the horizontal winds from ARPEGE
972 averaged over the same period. In order to highlight the CH_4 horizontal gradients, the range of the
973 colour scale changes from top to bottom.

974

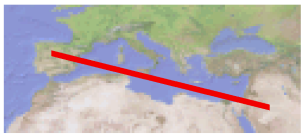

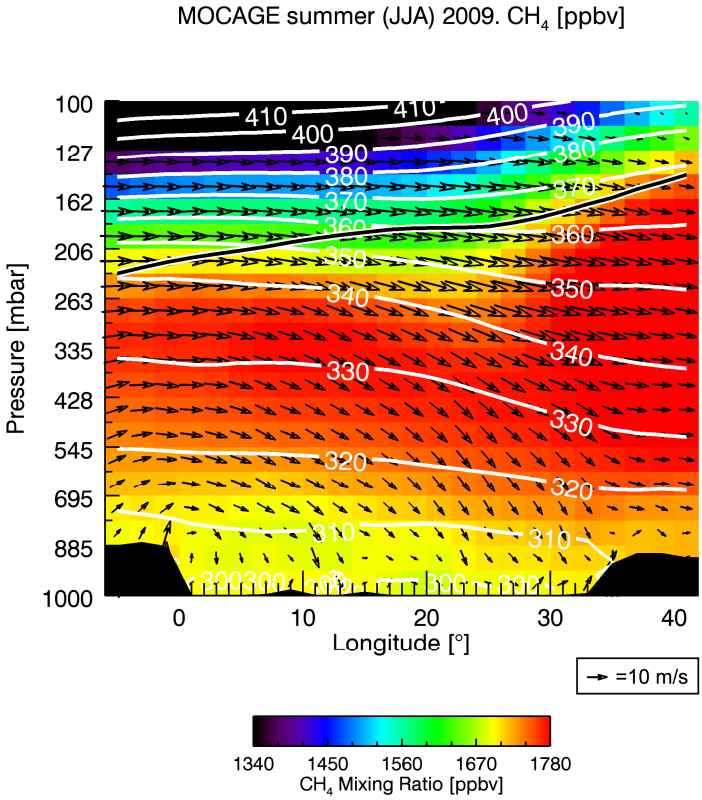

975

976 **Figure 2.** Vertical distribution of CH_4 as calculated by MOCAGE and averaged for JJA 2009 as a
977 function of longitude along the red line represented above the Figure. Superimposed are the
978 associated longitudinal and vertical winds from ARPEGE, together with the isentropes (white lines)
979 and the cold point tropopause from NOAA NCEP/NCAR reanalyses (black line) averaged over the
980 same period.

981

982

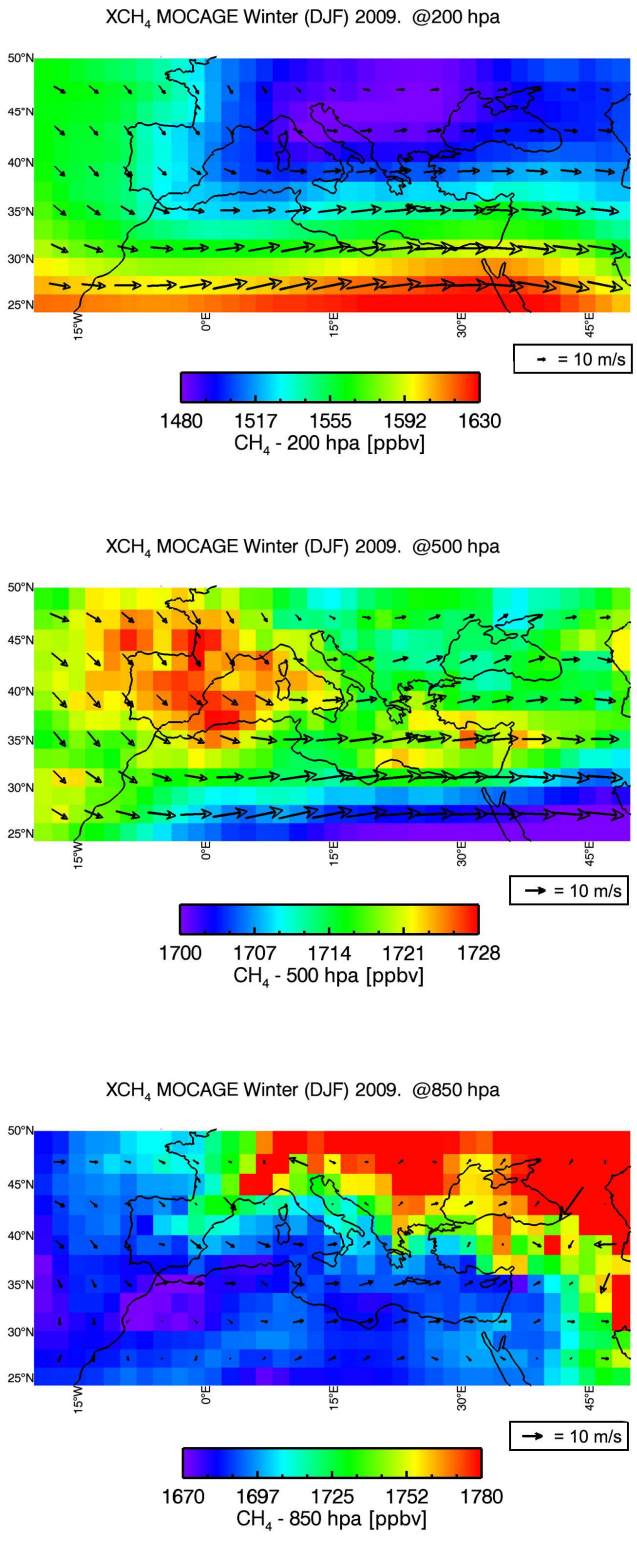

982

983 **Figure 3.** Same as Fig. 1, but for winter (DJF) 2009.

984

985

985

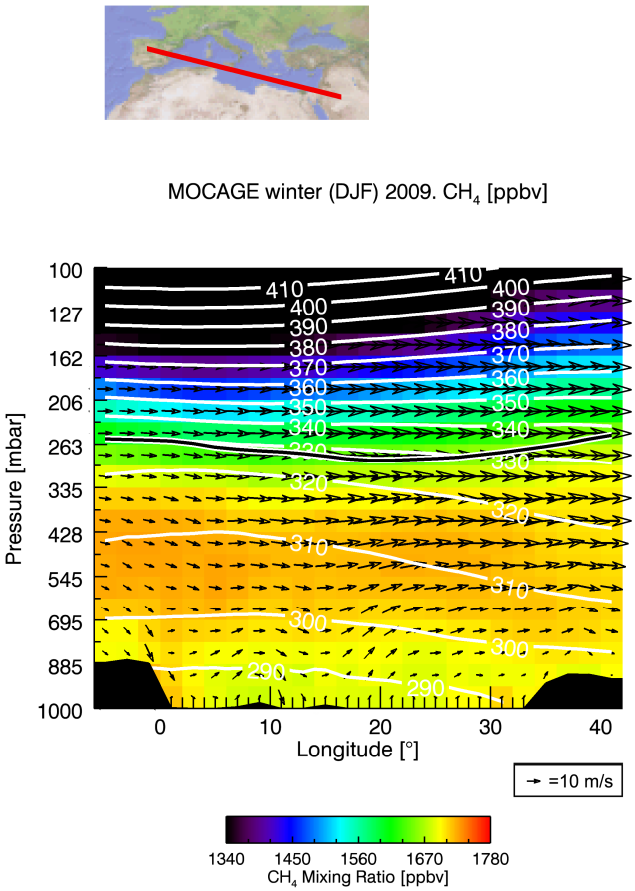

986

987 **Figure 4.** Same as Fig. 2, but for winter (DJF) 2009.

988

989

989

990

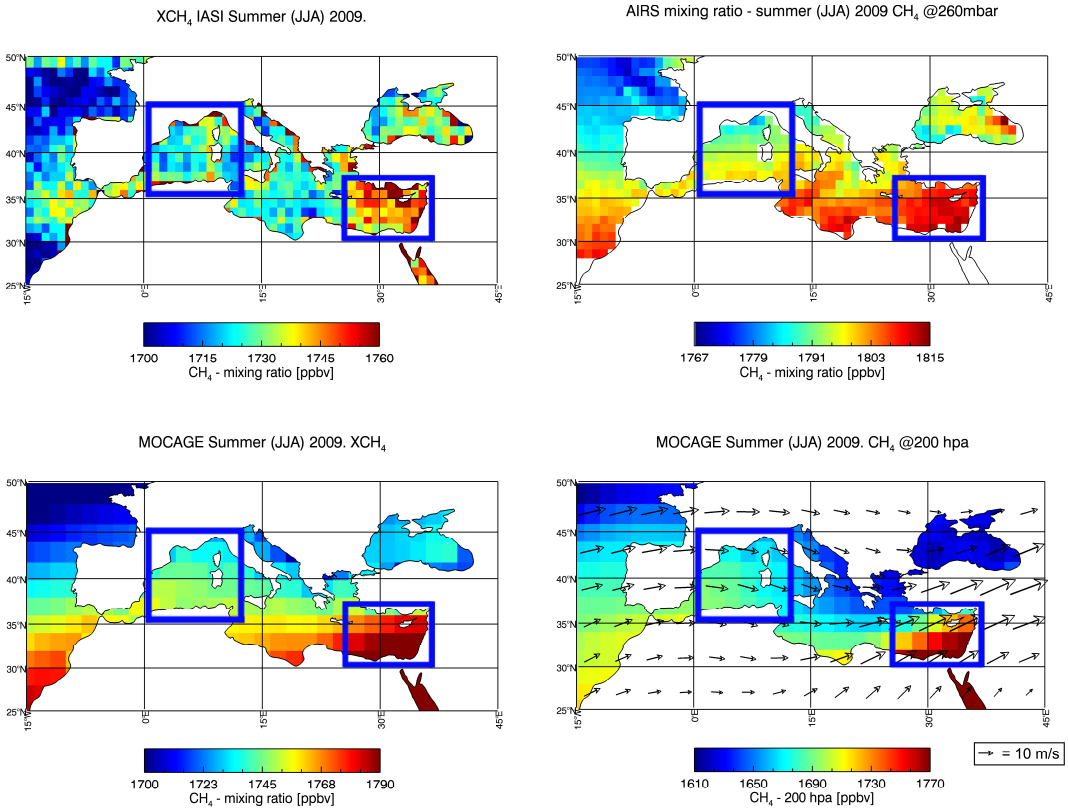

991

992 **Figure 5.** Field of total columns of CH_4 as measured by IASI and averaged for summer (JJA) 2009
993 (top left), and field of CH_4 at 260 hPa as measured by AIRS and averaged for JJA 2009 (top right).
994 (Bottom) Same as above but as calculated by MOCAGE. Satellite data are represented in a 1°x1°
995 resolution whilst model data are shown in a 2°x2° resolution. The two blue squares in the lower left
996 Figure represent the Western and Eastern Mediterranean Basins where the measured and modelled
997 data are selected over the Mediterranean Sea. Superimposed are the horizontal winds from
998 ARPEGE at 200 hPa averaged over the same period (bottom right). In order to highlight the CH_4
999 horizontal gradients, the range of the colour scale changes for each figure.

1000

1001

1001

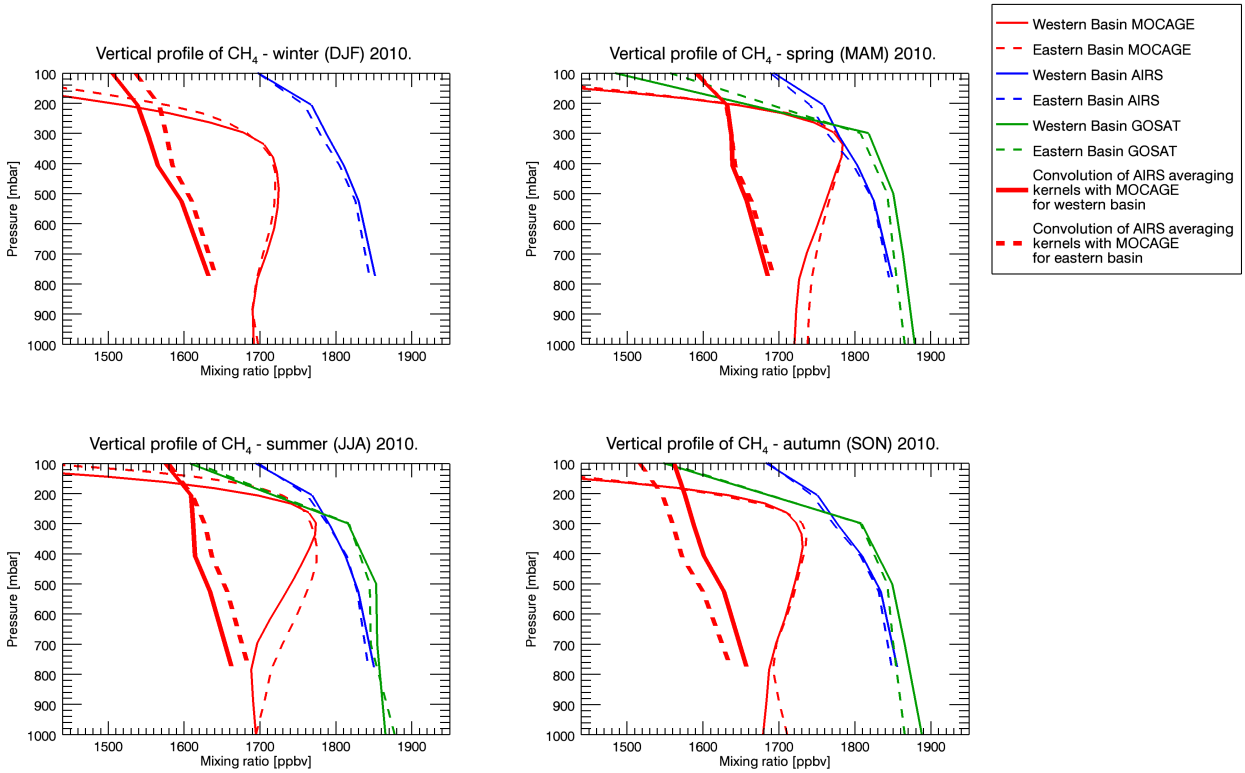

1002

1003 **Figure 6.** (From top to bottom and from left to right) Seasonally-averaged vertical profiles of CH_4
1004 as measured by AIRS (blue lines) and GOSAT (green lines), and as calculated by MOCAGE (thin
1005 red lines) over the Eastern (dashed lines) and Western (solid lines) MBs in winter, summer, spring
1006 and autumn 2010. Also shown are the seasonally-averaged MOCAGE profiles convolved with the
1007 AIRS averaging kernels (thick red lines) for the four seasons over the Eastern (dashed lines) and
1008 Western (solid lines) MBs.

1009

1010

1010

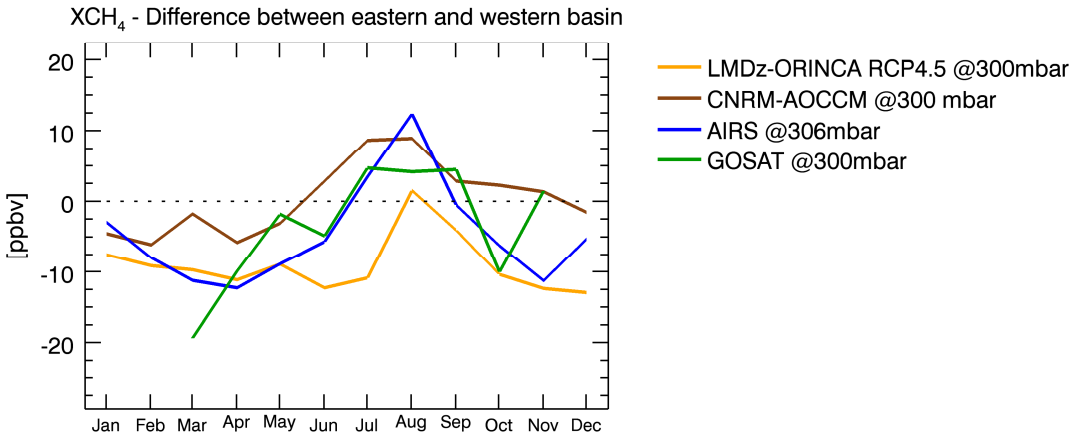

1011

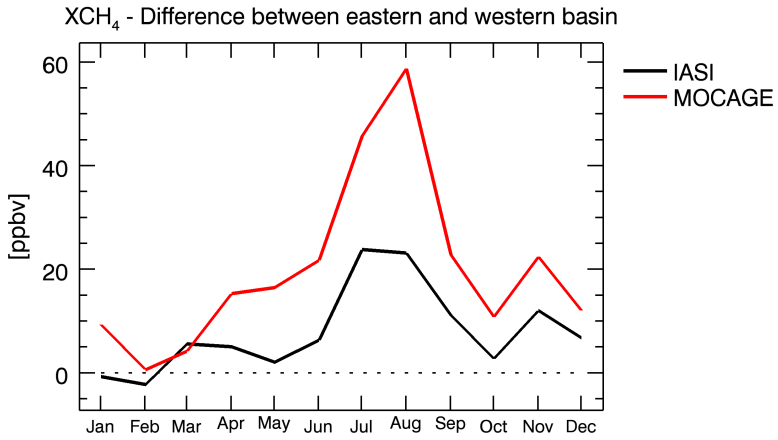

1012

1013 **Figure 7.** (Top) Seasonal evolution of the difference in the CH_4 fields between the Eastern and
1014 Western MB as measured by AIRS (blue line) and GOSAT (green line) at 306 and 300 hPa,
1015 respectively and as calculated by LMDz-OR-INCA (yellow line) and CNRM-AOCCM (brown
1016 line). (Bottom) Seasonal evolution of the difference in the CH_4 total columns between the Eastern
1017 and Western MB as measured by IASI (black line) and as calculated by MOCAGE (red line). The
1018 LMDz-OR-INCA and CNRM-AOCCM data sets cover the climatological period 2001-2010. The
1019 MOCAGE and IASI data sets cover the period 2008-2011 whilst the satellite AIRS and GOSAT
1020 data sets are representative of the year 2010.

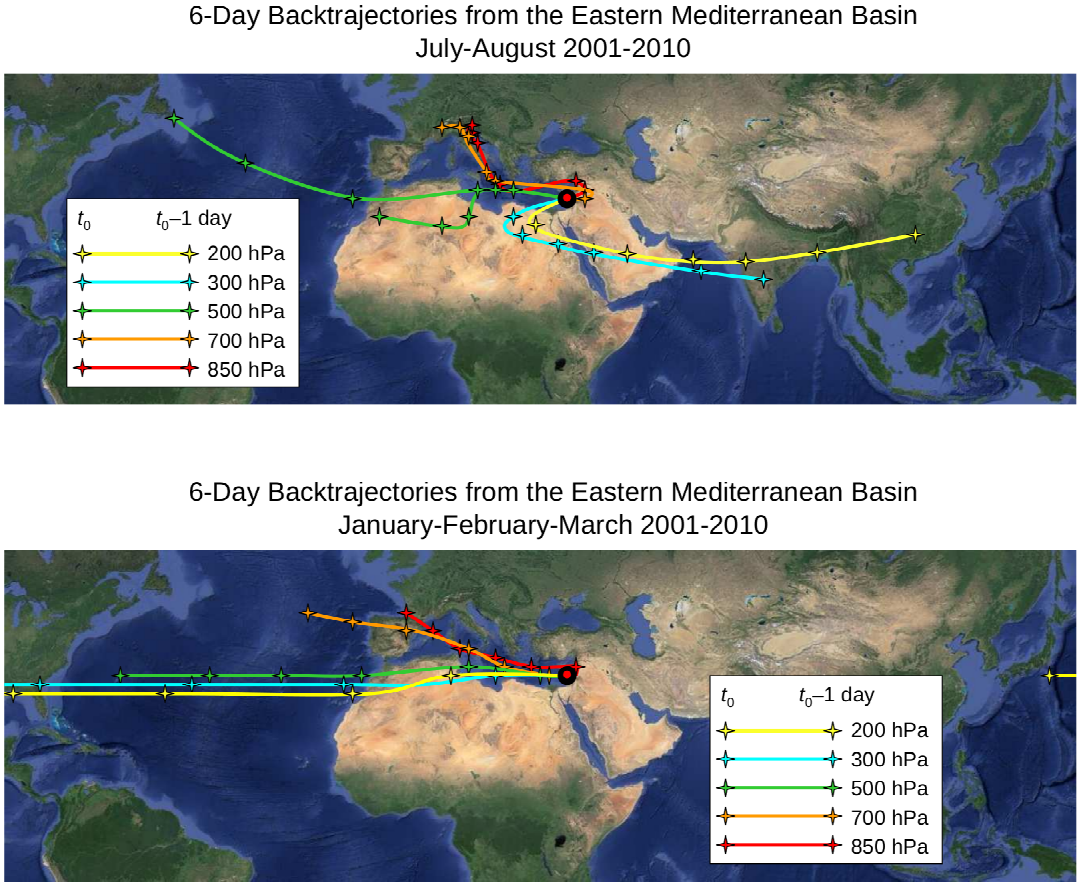

Figure 8. (Top) Climatological six-day back-trajectories from the point at 33° N, 35° E located in the Eastern Mediterranean Basin (red filled circle) calculated from the British Atmospheric Data Centre trajectory service (http://badc.nerc.ac.uk/community/trajectory/) from 1st July to 31st August from 2001 to 2010 every 12 hours at 850 (red line), 700 (orange line), 500 (green line), 300 (blue line) and 200 hPa (yellow line). The position of the gravity center of each distribution at each level is represented every 24 hours by a star. (Bottom) Same as top, but calculated from 1st January to 31st March 2001-2010.

1030

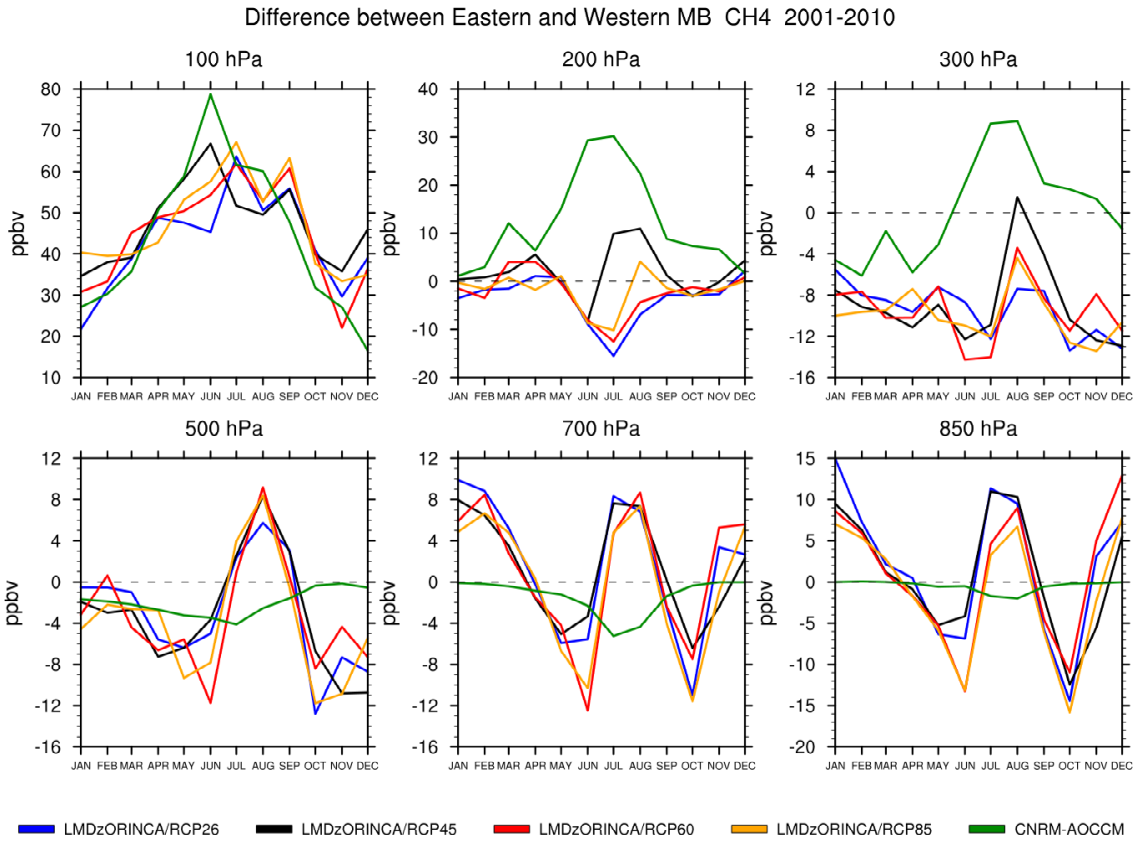

1031

1032 **Figure 9.** (From top to bottom and from left to right) Seasonal evolution of the difference in the

1033 CH_4 fields between the Eastern and Western MB over the climatological period 2001-2010 at 100,

1034 200, 300, 500, 700 and 850 hPa as calculated by CNRM-AOCCM (green) model and LMDz-OR-

1035 INCA according to the 4 IPCC scenarios: RPCs 2.6 (blue), 4.5 (black), 6.0 (red) and 8.5 (yellow).

1036 See section 2.2 for more details.

1037

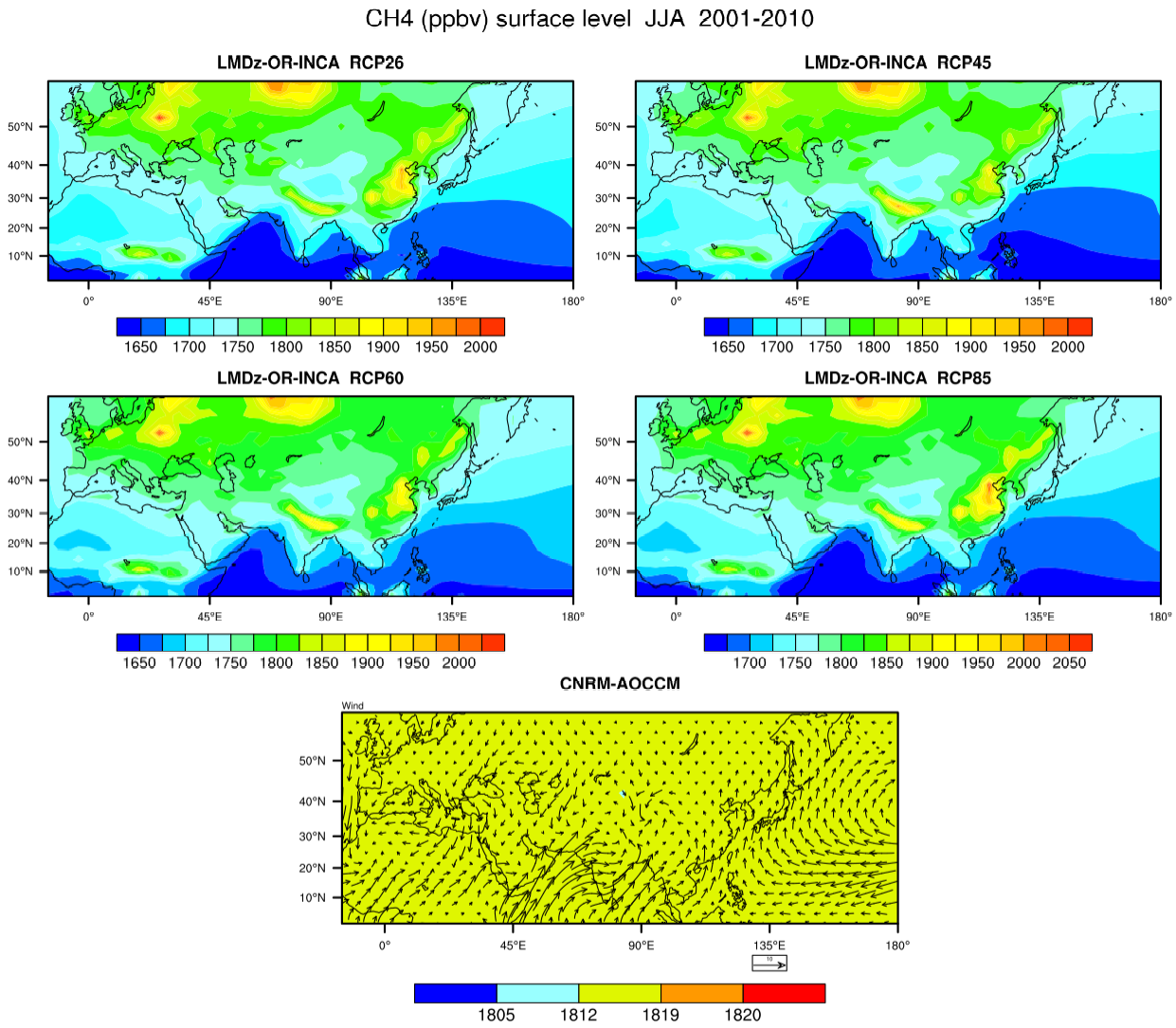

1038

1039 **Figure 10.** Fields of surface CH_4 as calculated by the CNRM-AOCCM model (bottom) and the
1040 LMDz-OR-INCA model (top and centre) according to the 4 IPCC scenarios (RCPs 2.6 (top left),
1041 4.5 (top right), 6.0 (centre left) and 8.5 (centre right)) averaged over the summer season (JJA) and
1042 the climatological period 2001-2010. Superimposed to the CNRM-AOCCM CH_4 fields (bottom) is
1043 the wind field at the surface averaged over the same period. Note that the range of the colour scale
1044 changes for each figure and that the surface CH_4 for CNRM-AOCCM (bottom) is constant.

1045

1046

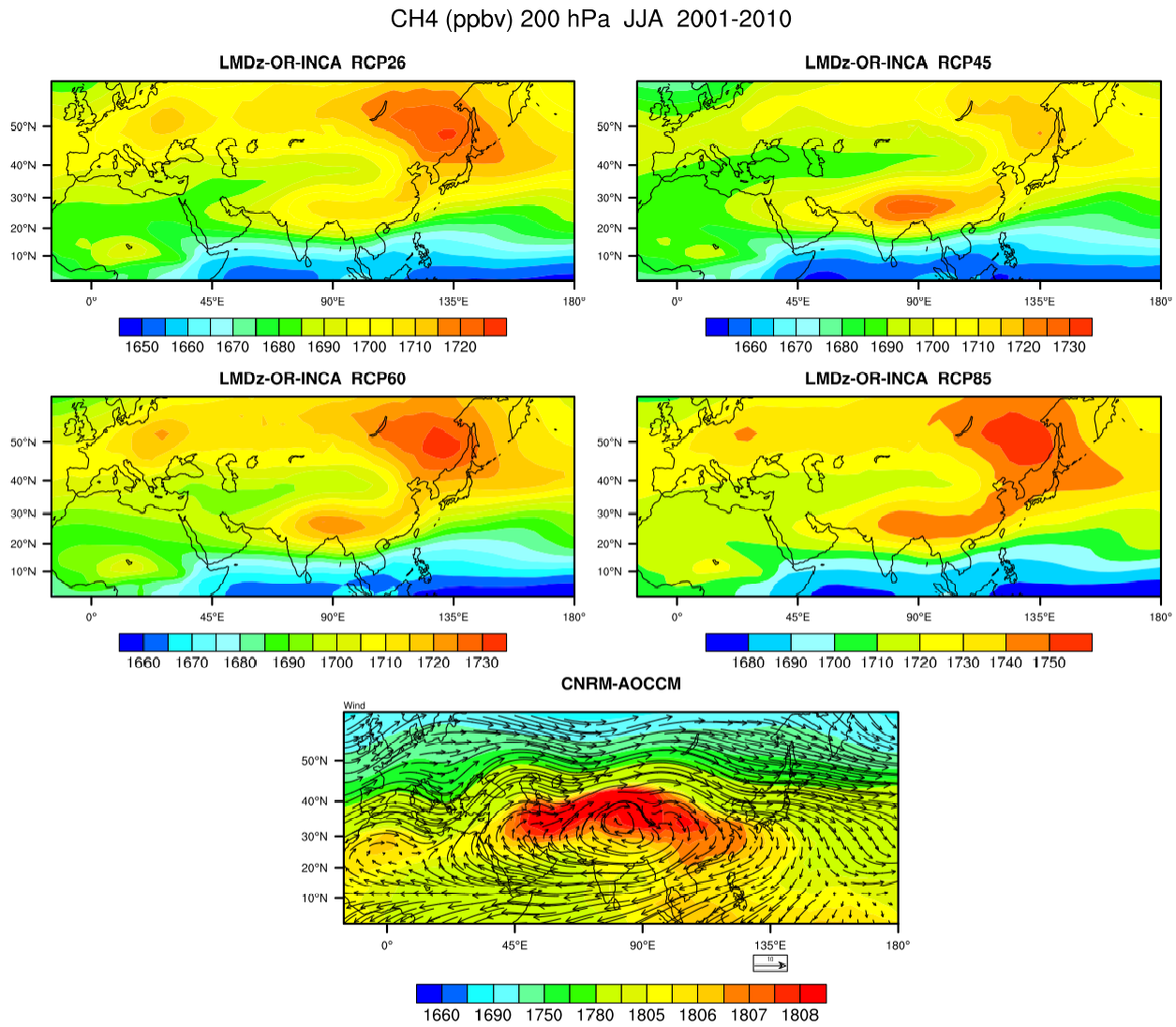

1046

1047 **Figure 11.** Fields of CH_4 as calculated by the CNRM-AOCCM model (bottom) and the LMDz-OR-
1048 INCA model (top and centre) considering the 4 IPCC scenarios (RCPs 2.6 (top left), 4.5 (top right),
1049 6.0 (centre left) and 8.5 (centre right)) at 200 hPa averaged over the summer season (JJA) and the
1050 climatological period 2001-2010. Superimposed to the CNRM-AOCCM CH_4 fields (bottom) is the
1051 wind field at 200 hPa averaged over the same period. Note that the range of the colour scale
1052 changes for each figure and that the colour scale for the CNRM-AOCCM model (bottom) is non
1053 linear.

1054

1055

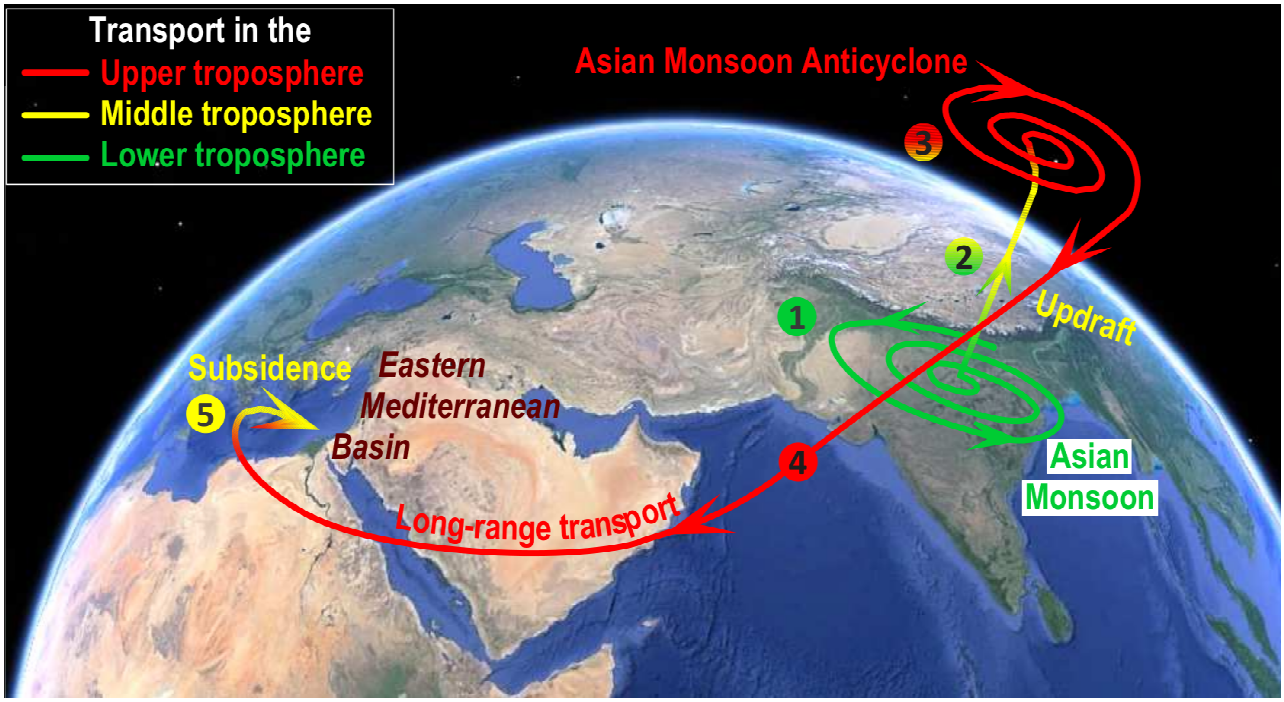

Figure 12. Schematic representation of the processes impacting the mid-to-upper tropospheric pollutants, including CH_4, above the Eastern Mediterranean Basin in summer (July-August). (1) Trapping of lower tropospheric pollutants in the Asian monsoon. (2) Updraft of pollutants in the Asian monsoon up to the upper troposphere. (3) Build-up of pollutants within the Asian monsoon in the upper troposphere. (4) Large-scale re-distribution of pollutants by the Asian Monsoon Anticyclone to the Middle East and North Africa in the upper troposphere. (5) Build-up of pollutants though descent down to the middle troposphere above the Eastern Mediterranean Basin.